SAE INTERNATIONAL

Modeling Ignition and Premixed Combustion Including Flame Stretch Effects

2017-01-0553

Published 03/28/2017

Lorenzo Sforza, Tommaso Lucchini, and Angelo Onorati
Politecnico di Milano

Xiucheng Zhu and Seong-Young Lee
Michigan Technological University

CITATION: Sforza, L., Lucchini, T., Onorati, A., Zhu, X. et al., "Modeling Ignition and Premixed Combustion Including Flame Stretch Effects," SAE Technical Paper 2017-01-0553, 2017, doi:10.4271/2017-01-0553.

Abstract

Objective of this work is the incorporation of the flame stretch effects in an Eulerian-Lagrangian model for premixed SI combustion in order to describe ignition and flame propagation under highly inhomogeneous flow conditions. To this end, effects of energy transfer from electrical circuit and turbulent flame propagation were fully decoupled. The first ones are taken into account by Lagrangian particles whose main purpose is to generate an initial burned field in the computational domain. Turbulent flame development is instead considered only in the Eulerian gas phase for a better description of the local flow effects. To improve the model predictive capabilities, flame stretch effects were introduced in the turbulent combustion model by using formulations coming from the asymptotic theory and recently verified by means of DNS studies. Experiments carried out at Michigan Tech University in a pressurized, constant-volume vessel were used to validate the proposed approach. In the vessel, a shrouded fan blows fresh mixture directly at the spark-gap generating highly inhomogeneous flow and turbulence conditions close to the ignition zone. Experimental and computed data of gas flow velocity profiles and flame radius were compared under different turbulence, air/fuel ratio and pressure conditions.

Introduction

The numerical modelling of Spark-Ignited (SI) premixed combustion is a primary issue in the context of a more efficient and less pollutant automotive and heavy-duty engines. In fact, a detailed numerical description of the combustion process that takes into account all the involved effects (the properties of the ignition system, the local flow conditions and the combustible mixture features) allows to improve engines design and development with greater effectiveness.

Over the years, increasingly detailed numerical approaches were proposed, according to enhanced computational and experimental tools but also to more and more stringent engine design requirements. In the early nineties of the last century, Herweg and Maly [1] proposed the first idea of comprehensive model for SI engine combustion. In their work the development of a one-dimensional time-dependent single flame kernel is described considering, through different sub-models, the supplied electrical energy form the spark, the heat lost at the electrodes, the mean flow/turbulence effects (including the stretch phenomenon) and the contribution of chemical reactions. Later, in the first decade of the twenty-first century, improved comprehensive models where proposed by Reitz [2], Colin [3] and Bianchi [4]. The first one exploits a Lagrangian approach to track the early flame kernel, where particle markers are placed on the initial flame surface (assumed spherical) and moved in the radial direction with velocities that depends on heat transfer from the electrical circuit, laminar flame speed and local turbulence. The second one introduces a detailed model for the electrical circuit, where also the restrike phenomenon is considered, and takes advantage of a cloud of Lagrangian particles, each one representing a possible ignited flame kernel, for the plasma channel description. The third one uses improvements for the electrical circuit modelling similar to Colin's ones adopting, instead, a 1D single-particle approach for the early flame kernel evolution. A limitation for this expansion is introduced when the kernel radius reaches the value of 2 mm in order simulate the fully turbulent flame only with the main Eulerian combustion model. In fact Bianchi's model, as Reitz and Colin's ones, exploits the coupling *Lagrangian particles – Eulerian flame model* only to improve the ignition stage description, leaving the prediction of the further flame propagation to the main Eulerian model (for example the Extended Coherent Flame Model – ECFM [5], used with success by all described models). At the beginning of the 2010s, Dahms [6, 7, 8] and Lucchini [9-10] used similar techniques to manage the ignition stage in their comprehensive models for SI combustion, confirming the strength of the coupled Lagrangian-Eulerian approach. Both models exploit a linear path of particles, positioned along the spark-gap centerline, to simulate in more detail the shape of the plasma channel. In this way, the modeling of spark channel motion and elongation considers properly the local effects of flow and turbulence, improving the prediction of restrikes and local ignition events due to possible stratifications of mixture properties. The flame stretch effect, namely the strain rate introduced by turbulence and curvature effects on the flame, is

considered in the early Lagrangian flame kernel development by both models. In this context, Dahms includes also non-unity Lewis number effects through the computation of an effective Lewis number for the mixture. Differently from the former proposed comprehensive SI models, Dahms and Lucchini implemented for the Eulerian turbulent flame description the G-equation model [11] and the Coherent Flame Model (CFM) [12], respectively. Finally, Fansler [13] recently analyzed how advanced and detailed comprehensive models for SI combustion can be used not only to describe the ignition and the further flame development in the context of a Port Fuel Injection (PFI) strategy, but also with more recent configurations like Spary-Guided Stratified-Charge (SGSC) engines operated at part load with highly stratified fuel-air-residual mixtures.

Despite different modeling strategies, all the presented comprehensive models show good results when compared to experimental findings. However, under highly inhomogeneous flow condition at the spark-plug, the strain effects that turbulent eddies and curvature radius generate on the flame, namely the flame stretch effects, cannot be properly considered if included in a Lagrangian kernel growth approach coupled with a relatively coarse mesh. As well known, flow and turbulence stratifications at the ignition zone can be fully detected only if the local mesh is sufficiently refined. This condition leads to problems when chemical contribution, with flame stretch effects, are included in the Lagrangian particles evolution. In fact, when a particle becomes larger than a few cells the strain effects due to turbulence and curvature over a relatively large portion of the flame front are computed with respect to not only the same cell (where the particle center is positioned) but also considering values far from the actual flame front position. Moreover, recent DNS studies [14] about premixed flames propagation underline that the flame speed in presence of multidimensional and unsteady flows is a local property, and consequently the related stretch effects, which take a role in its computation, should be evaluated at the flame front position.

This paper describes a modified strategy to include flame stretch effects into the Eulerian-Lagrangian model for premixed SI combustion proposed by Lucchini [9-10], in order to describe ignition and flame propagation under highly inhomogeneous flow conditions. This is performed by fully decoupling the effects of the electrical circuit, in terms of thermal energy transferred to the gaseous mixture, from the computation of the laminar/turbulent flame speed. The Lagrangian particles are no more considered as possible ignited flame kernels, but they only generate an initial burnt field into the computational domain according to the energy transfer from the electrical circuit. Consequently, they are still introduced along the spark-gap centerline to model the evolution of the plasma channel geometry under local flow conditions, allowing the prediction of possible restrike events and different thermal energy deposition into the mixture. On the other side, the laminar/turbulent flame speed is evaluated directly by the main Eulerian Computational Fluid Dynamic (CFD) solver for a better description of local fields variations. In this context, a flame stretch model derived by asymptotic theories [15-16] and verified by recent DNS studies [14] was included in the Eulerian solver with the purpose to improve the flame speed prediction by the use of local values for the mean flow velocity, turbulence, curvature and Lewis number. The prediction of an effective Lewis number for a premixed mixture was introduced following the idea of Joulin and Mitani [17]. In addition, the electrical circuit modeling was modified, in order to predict properly restrike events and obtain the consequent current and voltage trends. Finally, the proposed approach was validated on experiments carried out at Michigan Tech University in a pressurized, constant-volume vessel [10]. In this configuration, a shrouded rotating fan coupled with a guide tube generates directly to the ignition zone a jet of fresh mixture with highly inhomogeneous flow and turbulence conditions. CFD simulations were performed using the open-source platform OpenFOAM® with suitable libraries (Lib-ICE) developed for combustion modeling.

In the following sections, first the proposed numerical modeling strategy to include flame stretch effects and all performed improvements for the selected Eulerian-Lagrangian model were explained in detail. Then, after a description of the experimental and numerical setup, the analysis of non-reacting flow velocity profiles at the ignition zone was carried out by a comparison with PIV experimental measurements. Hence, combustion tests were analyzed in order to assess the validity of the proposed improvements; experimental findings about flame radius were compared with numerical results under different turbulence, air/fuel ratio and pressure conditions. Finally, some conclusions and possible future developments were described.

Numerical Modeling Strategy

The SI premixed combustion is a phenomenon affected by several contributions, like the electrical circuit type and features, the local flow conditions, and the mixture properties. In particular, the ignition event and the overall initial stage of combustion need strong modeling efforts because all the aforementioned contributions compete together for the possible generation of a self-sustained fully turbulent flame or produce a misfire event.

Therefore, the comprehensive model proposed by Lucchini [9-10] was chosen as basic strategy to model combustion. This choice was achieved because its Eulerian-Lagrangian approach, joint with several sub-models, allows to consider correctly all the involved effects and to model the plasma arc as close as possible to its original geometry. In fact, especially under highly inhomogeneous flow conditions at the spark-gap, a correct representation of the electric arc is fundamental to properly simulate both its elongation and corrugation.

In this context, a novel approach to consider the flame stretch effects was introduced. The Lagrangian particles, whose role is to simulate the spark evolution, were no more considered as possible ignited flame kernels but only as portions of the electric arc where the introduced thermal energy should be deposited. On the other hand, the laminar/turbulent flame evolution, including flame-turbulence interactions, curvature effects and chemical contributions, was modeled only by the main Eulerian CFD code. At this level, a suitable model considers the flame stretch effects as function of the local flame front conditions of curvature, flow velocity, turbulence and Lewis number. The Lagrangian and Eulerian approaches are still coupled at each time-step, but only to allow the following conditions:

1. The particles must be affected by the local distribution of flow velocity, turbulence and pressure.

2. The Eulerian combustion code needs to be initialized by a burnt field, created by the transferred thermal energy and function of the electrical circuit properties.

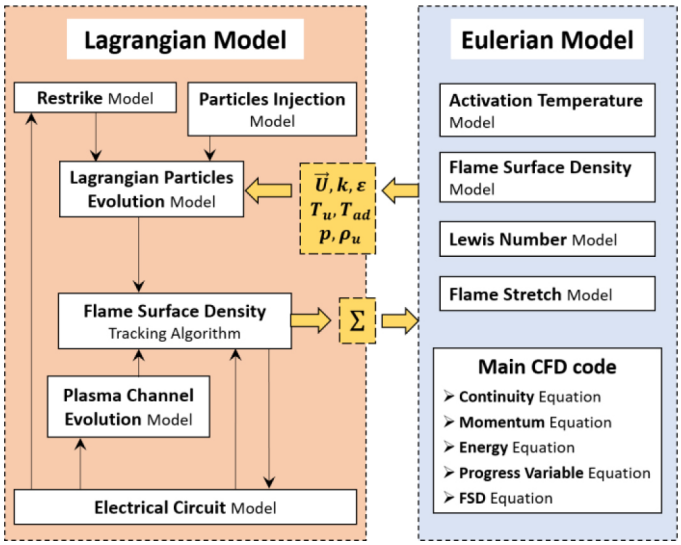

Figure 1. Scheme of the modified Eulerian-Lagrangian model.

Finally, modifications with respect to the original implementation concerned also:

1. The effective Lewis number prediction, in order to take into account possible non-unity Lewis number effects as thermal-diffusive instabilities of the laminar flame.
2. The electrical circuit modeling, to improve the prediction of possible restrike events and the achievement of proper current and voltage trends.

The result is the comprehensive model described schematically by Figure 1. In the next sub-sections all the sub-models used by both Lagrangian and Eulerian approaches (Figure 1) will be described in detail, focusing in particular on performed modifications.

Lagrangian Model

In the original and basic version [9], the Lagrangian model evolves particles considering not only the thermal effects of the electrical circuit but also the contribution of chemical reactions. In the following modified version, this last aspect was fully transferred to the Eulerian model removing from the Lagrangian particles evolution any influence of the laminar/turbulent flame speed parameter. The use of sub-model for:

1. Particles injection
2. Particles evolution
3. Plasma channel evolution
4. Electrical circuit
5. Restrike
6. Flame surface density tracking

was maintained (Figure 1) and improvements were carried out for the electrical circuit model. The Lagrangian model was coupled at each time-step with the Eulerian model to allow mutual influence.

Particles Injection Model

As in previous implementations [9-10], among the three characteristic stages of ignition in SI engines, namely breakdown, arc and glow discharge, only the last two were modeled because of the negligible duration of the first one. At spark time, and after any possible restrike event, a set of 10 Lagrangian particles were introduced along the spark-gap centerline, with the purpose to model properly the spark-channel geometry and its interaction with the local flow conditions. The particles were initialized in terms of temperature T_i and diameter d_i using the following relations [18-19]

$$T_i = \left[\frac{1}{k}\left(\frac{T_{bd}}{T_u} - 1\right) + 1\right] T_u \tag{1}$$

$$d_i = 2\left[\frac{k-1}{k}\frac{E_{bd}}{p\, d_{gap}\left(1 - \frac{T_u}{T_i}\right)\pi}\right]^{\frac{1}{2}} \tag{2}$$

which exploit the breakdown stage features to provide an initialization of the arc stage. In particular, T_{bd} is the breakdown temperature (chosen equal to 60000 K, as suggested by Refael [18]), k = 1.66 is the plasma channel specific heat ratio, T_u the unburned gas temperature, d_{gap} the inter-electrode distance, p the gas pressure and E_{bd} the breakdown energy. This last value is computed by the electrical circuit model and assumes different values depending on the ignition event type (if *first ignition* or *restrike*), as it will be explained further in detail.

Lagrangian Particles Evolution Model

The particles introduced in the computational domain at spark time, or after any restrike event, were evolved considering the following three phenomena:

1. The convection imposed by the flow field distribution at the spark-gap.
2. The heat transferred by the hot plasma channel, generated during the breakdown stage, to the fresh surrounding mixture.
3. The heat released by the ignition system.

To take the convection from the gas flow into account, the equation [9]:

$$\frac{d\boldsymbol{x}_p}{dt} = \boldsymbol{U}_g \tag{3}$$

was solved for each particle, where $\boldsymbol{x}_p$ is the particle position vector and $\boldsymbol{U}_g$ is the local gas velocity. This last parameter was interpolated at the particle position adopting the *cell-point-face* technique [20], with the purpose to reduce the dependency of the computed channel motion from the adopted mesh size. On the other hand, additional random contribution of local turbulence intensity were neglected from Eq. 3 to ensure a reasonable spark channel evolution.

The initial hot plasma channel evolution and the further effect of the heat transfer from the electrical circuit were modelled by solving the mass conservation

$$\frac{dm_p}{dt} = 4\pi\, r_p^2\, \rho_k\, s_{plasma} \tag{4}$$

and the radius variation

$$\frac{dr_p}{dt} = s_{plasma} + s_{therm} \tag{5}$$

equations, where m_p, r_p and ρ_k are the particle mass, radius and density, respectively. The equations 4 and 5 include no more the effects of the chemical reactions, as in the original model version [9-10], but only the following contributions are considered:

1. Generation of an initial burnt field by the plasma channel fast expansion towards the surrounding fresh mixture (s_{plasma}).
2. Thermal support of the created spark-channel (s_{therm}).

The treatment of these different phenomena, and the consequently computation of s_{plasma} and s_{therm}, was carried out considering that:

1. The plasma channel expansion is experienced only at very high temperature conditions and under non-uniform temperature distribution inside the channel.
2. The thermal support available from the electrical circuit becomes important only when the spark channel temperature decreases and the plasma expansion tends to disappear. With such conditions inside the channel, the temperature can be assumed uniform and the composition at chemical equilibrium.

Therefore, these two mechanisms were modelled according to different approaches and a temperature threshold value of $3T_{ad}$ [4, 9, 10, 21], where T_{ad} is the adiabatic flame temperature, was used to switch from the first to the second one. Hence when the particle temperature T_p is:

1. $T_p > 3T_{ad}$, the plasma channel fast expansion governs the particle evolution and a suitable model (the plasma channel evolution model) computes the heat conduction inside the channel and the growth velocity s_{plasma}.
2. $T_p < 3T_{ad}$, the thermal support of the spark channel from the electrical circuit becomes relevant and the plasma expansion contribution (s_{plasma}) can be neglected. Consequently, the s_{therm} value for each particle is achieved by the resolution of an energy conservation equation under the hypothesis of uniform temperature and chemical equilibrium composition inside the channel.

For what concerns the s_{therm} computation, the following equation was used [9]

$$s_{therm} = \frac{V_p}{A_p}\left(\frac{1}{T_p}\frac{dT_p}{dt} - \frac{1}{p}\frac{dp}{dt}\right) \tag{6}$$

in which V_p and A_p are the particle volume and surface, while p is the pressure. The particle temperature variation dT_p/dt was obtained solving the energy conservation equation

$$\frac{dT_p}{dt} = -\frac{\dot{m}_p}{m_p}\left(T_p - T_{ad}\right) + \frac{\dot{Q}_{spk_P}}{m_p\, c_p} + \frac{1}{\rho_k\, c_p}\frac{dp}{dt} \tag{7}$$

with c_p being the specific heat and $\dot{Q}_{spk_P}$

the energy deposition rate from the electrical circuit to the particle, reduced of the heat losses. This last term was computed as follows

$$\dot{Q}_{spk_P} = \frac{\dot{Q}_{spk}\,\eta_{eff}}{n_{particles}} \tag{8}$$

where $\dot{Q}_{spk}$ and η_{eff} are the total heat transfer rate from the electrical circuit to the gas phase and the efficiency of this energy deposition, respectively, while $n_{particles}$ is the number the Lagrangian particles introduced along the spark gap and on which the thermal energy is distributed.

Finally, the Lagrangian particles evolution was interrupted upon the occurrence of one of the following possibilities:

1. Restrike event, because a new conductive path is generated between the electrodes, with the consequent introduction and evolution of a new set of particles.
2. Electrical circuit energy complete consumption, because no more energy is available for creation and/or support of any spark channel.

This modelling strategy, strictly coupled with the Eulerian flame evolution, allows also to take into account of possible misfire events in case of the electrical circuit incapability to generate a self-sustained flame kernel. This possibility could be verified, for example, in presence of too low available energy at the secondary circuit or unfavorable flow conditions at the spark-gap.

Plasma Channel Evolution Model

Until the evolved Lagrangian particles satisfy the condition $T_p > 3T_{ad}$, the heat conduction from the hot plasma channel to the surrounding fresh mixture, which allows the creation of an initial fully burnt field, cannot be neglected. Therefore, the non-uniform temperature distribution inside the channel and its consequent growth rate (s_{plasma}) need to be modelled in detail, taking into account for actual plasma properties.

As performed by Lucchini [9], all the tracked particles satisfying the condition $T_p > 3T_{ad}$ were assumed to have the same temperature distribution, computed by solving with a sub-cycle procedure the heat conduction equation for the space-dependent plasma temperature T_{pl}

$$\frac{dT_{pl}}{dt} = \alpha_{pl}\,\nabla^2 T_{pl} + \frac{\dot{Q}_{spk}\,\eta_{eff}}{\rho_{pl}\, c_{p,pl}\, V_{pl}} \tag{9}$$

over a 1D axisymmetric mesh, representing a wedge of the gas region around the spark-gap centerline. In Eq. 9, α_{pl}, ρ_{pl}, $c_{p,pl}$ and V_{pl} are the thermal diffusivity, density, heat capacity and volume of the plasma channel, respectively. These properties were estimated employing the functions provided in [22] and assuming chemical equilibrium conditions [9], in order to take into account dissociation of molecules

and atom ionization effects. Then, as suggested by Herweg and Maly [1], at each time step the plasma channel radius r_k, namely the end of the burnt field imposed over the 3D computational domain by the channel presence, is identified by the location on the 1D wedge mesh where the adiabatic flame temperature T_{ad} is detected. Hence, the s_{plasma} was computed as [9]

$$s_{plasma} = \frac{r_k(t + \Delta t) - r_k(t)}{\Delta t} \tag{10}$$

with Δt being the CFD simulation time-step.

Electrical Circuit Model

The capability to estimate the evolution of the main parameters of the adopted electrical circuit, since the spark time until the complete consumption of the stored energy, allows a detailed description of the energy transfer process to the fresh mixture through the generated spark channel. This is fundamental for a correct initialization of the burnt field in the Eulerian computational domain, especially under highly inhomogeneous flow conditions, lean mixtures and high turbulence/laminar flame speed ratios, in order to predict the propagation of fully turbulent flame or a misfire event.

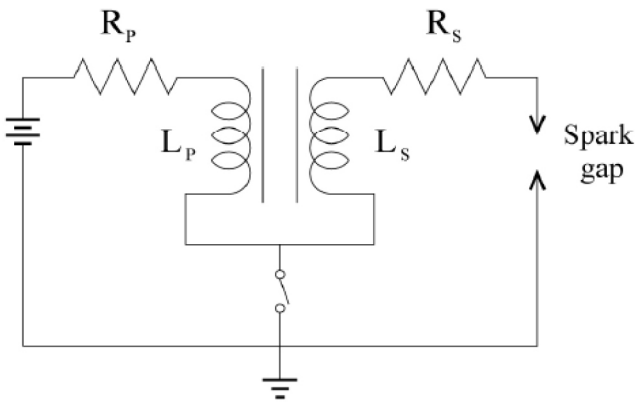

Figure 2. Simplified scheme of a classical inductive ignition system characterized by a primary (subscript P) and a secondary (subscript S) circuit. The parameters R and L represent the equivalent resistance and inductance of both circuits, respectively [9].

The usual behavior of a generic inductive ignition system for SI engines, characterized by a primary and a secondary circuit as shown by Figure 2, can be summarized schematically as follows:

1. When the primary circuit is closed, a battery generates a primary current i_P allowing the storage of energy inside the primary inductance L_P.
2. At spark time, the primary circuit is opened and the energy stored in L_P is transferred to the secondary circuit.
3. The secondary circuit dissipates by Joule effect through both the spark-gap ($V_{IE}(t)\ i_S(t)$, where V_{IE} is the inter-electrode voltage fall and i_S the secondary current) and its other dissipative devices ($R_S\ i_S^2(t)$, with R_S being the secondary resistance) the whole received energy.

Therefore, taking example from already used approaches [3, 9], a suitable model was implemented. The presence of a primary and a secondary circuit was considered (Figure 2), although only the last one was modeled in detail. In fact, once known the amount of energy stored in the primary circuit at spark time E_P (which depends on the charging time), the energy transferred to the secondary circuit E_S' and available for the breakdown stage was simply computed as

$$E_S' = c_{eff} E_P \tag{11}$$

Here, $c_{eff} \cong 0.6$ is the transmission coefficient, which models the secondary inductance L_S dissipations during the energy transfer from primary to secondary circuit and whose value is estimated by [3]. According to the performed Lagrangian particles injection and evolution, only arc and glow stages were modelled. Therefore, the breakdown stage effects were considered only as initial condition for the available energy at the beginning of arc stage by the computation of the breakdown energy E_{bd} as carried out in [3, 4]

$$E_{bd} = \frac{V_{bd}^2}{C_{bd}^2\ d_{gap}} \tag{12}$$

Here, C_{bd} is the breakdown constant, a parameter expressed in [kV/(mJ$^{1/2}$ mm$^{1/2}$)] and that needs to be calibrated, d_{gap} the inter-electrode distance in [mm] and V_{bd} the breakdown voltage in [kV]. This last parameter was computed as follows

$$V_{bd} = a + b\ \frac{p}{T_u} + c\ \frac{p}{T_u}\ d_{gap} \tag{13}$$

according to [4, 23]. The parameters a, b and c of Eq. 13 can assume different values depending if the modelled spark channel belongs to the first discharge (performed at the spark-time) or to any possible restrike phenomenon. The necessity of a variation for Eq. 13 parameters value can be deduced by:

1. comparing typical experimental values of V_{bd} for the first discharge ($V_{bd} \approx 5 \div 20\ kV$, [24]) and for possible restrike events ($V_{bd} \approx 1.5 \div 4\ kV$, [1, 24]), and
2. considering that during the ignition process T_u and d_{gap} are constant, while p could also increase.

For the first discharge, as reported in [4, 23], the parameters of Eq. 13 are the following: $a = 4.3\ kV$, $b = 136\ (kV\ K)/bar$ and $c = 324\ (kV\ K)/(bar\ mm)$.

Consequently, the available secondary circuit energy at the beginning of the arc stage was obtained from Eq. 11 and 12 as

$$\begin{cases} E_S(t = t_{spark-time}) = E_S' - E_{bd} & (a) \\ E_S(t = t_{restrike}) = E_S(t = t_{restrike}) - E_{bd} & (b) \end{cases} \tag{14}$$

where Eq. 14a is valid for the first discharge and Eq. 14b for any restrike, while the secondary circuit energy time variation was estimated as in [3]

$$\frac{dE_S(t)}{dt} = -R_S\ i_S^2(t) - V_{IE}(t)\ i_S(t) \tag{15}$$

Here, R_S assumes a constant value depending on the adopted electrical circuit type, while i_S and V_{IE} are time-dependent parameters computed at each time-step as

$$i_S(t) = \sqrt{\frac{E_S(t)}{L_S}} \tag{16}$$

and

$$V_{IE}(t) = V_{cf} + V_{af} + V_{gc}(t) \tag{17}$$

The parameter L_S of Eq. 16 is a constant feature of the circuit, similarly to R_S, while V_{cf}, V_{af} and V_{gc} of Eq. 17 are the cathode, anode and gas-column voltage falls, respectively, whose modelling strategy is described in detail in Appendix A.

Concerning the possibility to experience heat losses at the electrodes during the spark-discharge, the approach used in [1, 9] was followed. Hence, the computation of the parameter η_{eff}, already considered in Eqs. 8 and 9 and representing the efficiency of the energy transfer process from the electrical circuit to the gaseous mixture, was carried out according to

$$\eta_{eff} = \eta_0 + \frac{(\eta_\infty - \eta_0)\, U^3}{A + U^3} \tag{18}$$

The parameters η_0 and η_∞ represent the energy transfer efficiency under conditions of quiescent mixture and high velocity flow at the spark-gap (> 15 *m/s*), respectively; together with the constant A, they assume different values depending on the discharge stage (see Table 1). On the other hand, U is simply the average velocity of the introduced Lagrangian particles, computed as in [9].

Table 1. Parameters for η_{eff} computation. The parameters η_0 and η_∞ are in [%], while A is in [m^3/s^3], [9].

Parameter	Arc stage	Glow stage
η_0	36	8
η_∞	50	30
A	500	700

The proposed electrical circuit model was tested on the experimental data provided by Herweg and Maly [1] regarding two different electrical circuit systems:

1. the Transistor Coil Ignition System (TCI)
2. the Capacitor Discharge Ignition System (CDI)

The results were almost satisfactory, as showed in Appendix B.

Restrike Model

The restrike is a phenomenon that takes place when the inter-electrode voltage V_{IE} (Eq. 17) becomes higher than a threshold value, which can be called *restrike breakdown voltage* V_{bd} (Eq. 13 with suitable parameters *a*, *b* and *c*), and a new spark channel is created along the spark-gap centerline. This can usually be experienced when, after the first discharge, a local high value of the flow elongates the spark channel, increasing the gas-column voltage fall V_{gc} (Eqs. 17 and A.2) until the condition $V_{IE} > V_{bd}$ is reached (Figure 3a). This phenomenon was observed by experimental tests [24] and its correct prediction is fundamental, because the sequential creation of several spark channel under local high flow conditions significantly influences the flame kernel development of engines with organized charge motion (e.g.: tumble or swirl) into the cylinder.

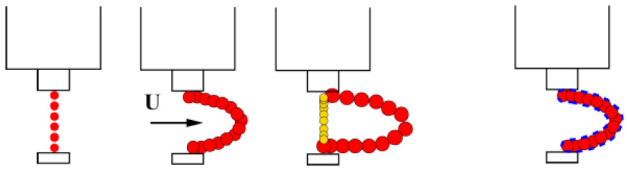

(a) (b)

Figure 3. The restrike phenomenon (a) and the flame surface tracking technique (b), [9].

The implemented model allowed the restrike prediction thanks to the combined used of Eqs. 13 and 17: when the condition $V_{IE} > V_{bd}$ was satisfied, a new set of Lagrangian particles was introduced between the electrodes. The particles representing the former spark channel were completely removed, in order to simulate the transition of the total heat transfer rate $\dot{Q}_{spk}$ to a new channel.

Flame Surface Density Tracking Algorithm

Following the approach proposed in [9] with the addition of some modifications, all the effects of the electrical circuit were introduced into the Eulerian domain through:

1. The computation of the flame surface density Σ.
2. The imposition of a fully burnt mixture inside the spark channel.

In fact, being Σ computed at each time-step, the flame kernel initialization performed on the Eulerian mesh by the ignition system was ensured. In particular, the Σ computation was carried out doing the following steps:

1. Placement of a spherical triangulated sphere at each particle position.
2. Variation of each triangulated sphere radius in order to match the related particle dimension.
3. Definition of flame surface as the total area of the non-intersecting triangular faces of the placed spheres (Figure 3b).
4. Definition of the number of non-intersecting triangular faces $N_{f,cell}$ inside each cell of the computational mesh.
5. Computation of Σ for each cell as $\Sigma_{cell} = \left(\sum_{i=1}^{N_{f,cell}} S_i\right)/V_{cell}$, where S_i is the area of the *i*-th triangular face.

At the same time, a completely burnt mixture was imposed into the mesh cells located inside the evolved Lagrangian particles, in order to simulate the initial burned field generated by the spark channel. In case of particles smaller than the cell size only a fraction of burnt mixture was imposed to each involved cell, namely only the actual volume inside the particles was considered fully burnt.

When a restrike event happened, or at the end of the electrical circuit energy, the particles evolved since that time were removed and their contribution in terms of both Σ and burnt field were no more updated on the computational mesh with Lagrangian model information. This allows to leave the prediction of possible misfire events to the Eulerian model, in particular because of stretch, in case the electrical circuit will not be able to sufficiently sustain the early flame kernel growth.

Eulerian Model

The *Eulerian Model* definition was used to group together all that modelling strategies implemented to work into an Eulerian framework, as the 3D computational mesh. Consequently, it was possible to define five "environments" interacting together and in which different operations were carried out (Figure 1):

1. The main CFD code
2. The flame surface density model
3. The flame stretch model
4. The Lewis number model
5. The activation temperature model

This Eulerian framework was coupled at each time-step to the Lagrangian model, in order:

1. to provide the flow field ($\vec{U}$, k, ε and p, with k, ε being the turbulence kinetic energy and its dissipation rate) and mixture (T_u, T_{ad} and ρ_u) quantities necessary for the evolution of the spark channel particles,
2. to receive information regarding the initial burnt field created by the spark discharge (Σ and the burnt mixture inside the channel).

A detailed description of the listed parts of the Eulerian model is provided in the following sub-sections.

Main CFD Code

The main CFD code is the environment that connects together all the implemented Eulerian sub-models. Its task is to manage the resolution of the flow field governing equations, namely the:

1. continuity,
2. momentum,
3. energy,
4. chemical species

ones, and the equations necessary for the laminar/turbulent flame modelling.

For this last topic, the Coherent Flamelet Model (CFM) proposed by Choi and Huh [12] was adopted, according to [9]. The model application was carried out by solving two transport equations:

1. the combustion normalized progress variable c,
2. the flame surface density Σ.

The source terms for the aforementioned equations were computed, respectively, as function of:

1. The unstretched laminar flame speed s_{u0}, the flame surface density Σ, and the stretch factor I_0, all suitable calculated for each cell of the computational domain.
2. The flame surface density Σ_{cell}, computed by the Lagrangian model during the spark discharge, and the flame surface density production P_{FSD} and destruction D_{FSD} terms, provided by the related model.

Flame Surface Density Model

The implemented flame surface density model provides the values of the production P_{FSD} and destruction D_{FSD} terms for the Σ equation resolution. Because the CFM model was used, these terms were computed as follows [9, 12]:

$$P_{FSD} = \alpha_{FSD} \frac{u'}{l_{tc}} \tag{19}$$

and

$$D_{FSD} = \beta_{FSD}\, s_{u0} \frac{\Sigma^2}{c\,(1-c)} \tag{20}$$

where α_{FSD} and β_{FSD} are model constants that need a suitable calibration, u' is the turbulence intensity and l_{tc} is a length scale introduced for dimensional reasons and set according to [12].

Flame Stretch Model

The unstretched laminar flame velocity s_{u0} can be computed by several correlations [25-26], like the Gülder one [27] which was used in this work, as function of the fuel type, the local equivalence ratio, the temperature and the pressure. However, the calculated value does not take into account of:

1. Curvature effects due to the flame front geometry (e.g.: a curved expanding flame).
2. Strain effects due to the *flame front*/*flow field* interaction.

These effects are grouped in a single physical process, called flame stretch, which has to be modelled for a correct laminar flame velocity estimation.

Following the approach proposed in [10], the actual laminar flame speed s_u was computed according to Bradley, Lau and Lawes [16]:

$$s_u = s_{u0} \frac{1 - K\,Ma}{1 + \frac{c}{R}\,\delta_l\,Ma} \tag{21}$$

with δ_l being the laminar flame thickness and c = 1 the parameter to fit Eq. 21 for cylindrical flame shapes. This choice was justified by the well-known knowledge that the flame stretch effects are predominant during the initial kernel growth stage, where the local

curvature effects are high. Hence, during this initial expansion, the flame has a similar shape to the modelled spark channel geometry, which is cylindrical.

The dimensionless Karlovitz stretch factor K was computed as in [15]

$$K = 0.157 \left(\frac{u'}{s_{u0}}\right)^2 R_L^{-0.5} \tag{22}$$

where $R_L = (u' L_i)/\nu$ is the turbulent Reynolds number, with L_i being the integral length scale of turbulence and ν the kinematic viscosity. The parameter $1/R$, known as the local flame curvature, was obtained on the Eulerian domain using the following relation

$$\frac{1}{R} = \left| \nabla \cdot \left(\frac{\vec{\nabla} c}{\left\| \vec{\nabla} c \right\|} \right) \right| \tag{23}$$

where $\vec{\nabla} c / \left\| \vec{\nabla} c \right\|$ is the flame front perpendicular direction.

Recent DNS studies [14] figured out that the flame speed is a local property when flows are multi-dimensional and unsteady, because the mass flow rate through the combustion region is not constant and varies through the flame. Consequently, its prediction under such conditions has to be completely carried out into an Eulerian framework, in order to avoid possible errors derived by a non-local approach. Moreover, in [14], the flame stretch formulation described by Eqs. 21, 22, 23 and obtained through an asymptotic analysis was tested against DNS results. The conclusions showed how the Bradley, Lau and Lawes approach must be applied using fields values evaluated over an isotherm sufficiently close to the flame burnt side. Therefore, considering that this work adopted a RANS turbulence modelling and the inner flame front is not resolved, fields value of fully burnt products in the flame brush region were used.

Hence, the Markstein number Ma of Eq. 21 was evaluated into fully burnt products according to [14]:

$$Ma = \left[\frac{1}{\gamma} \ln\left(\frac{1}{1-\gamma}\right) + \frac{1}{2} Ze(Le-1) \frac{1-\gamma}{\gamma} \int_0^{\frac{\gamma}{1-\gamma}} \frac{ln(1+x)}{x} dx \right] - \ln\left(\frac{1}{1-\gamma}\right) \tag{24}$$

where $\gamma = (\rho_u - \rho_b)/\rho_u$ is the expansion ratio, being ρ_b and ρ_u the burned and unburned density, respectively, x is a dummy variable of integration, and Ze is the Zel'dovich number, computed as [28]

$$Ze = \frac{T_{act}\,(T_{ad} - T_u)}{T_{ad}^2} \tag{25}$$

Both the Lewis number Le (Eq. 24) and the activation temperature T_{act} (Eq. 25) were evaluated by suitable models.

Lewis Number Model

In the context of premixed combustion, various instability modes can affect the flame front. One of these is the thermo-diffusive instability, which is controlled by the relative importance of the heat diffusion with respect to the deficient reactant one [29], namely by the Lewis number, defined as the ratio of these magnitudes. However, this definition of the Lewis number shows problems in presence of a stoichiometric mixture, where the deficient reactant cannot be clearly defined. Moreover, the Lewis number of a common hydrocarbon (like propane) can experience a steep variation of its value when computed following this approach for a mixture with equivalence ratio 0.9 or 1.1.

Joulin and Mitani [17] noticed from experiments that the flame behaviour gradually changes as the equivalence ratio varies across the stoichiometric condition. This means that the combustion process is controlled not only by the deficient component of the mixture, but also by the abundant one; consequently, also the effect on the flame stability of this last component should be considered.

Accordingly, the implemented strategy for the prediction of the Lewis number of a premixed mixture was that proposed in [17]:

$$Le = Le_{def} + H\left(Le_{abu} - Le_{def}\right) \tag{26}$$

where Le_{def} and Le_{abu} are the Lewis number defined with respect to the deficient and abundant reactant diffusivity, respectively. The parameter H is evaluated as

$$H = n \frac{G(m, n-1, A)}{G(m, n, A)} \tag{27}$$

with

$$G(m, n, A) = \int_0^{\infty} x^m \, (x + A)^n \, e^{-x} \, dx \tag{28}$$

Eqs. 27 and 28 are both function of m and n, which are the order of reaction of the deficient and abundant reactant. The value of A can be computed with the following expression

$$A = Ze \frac{y}{Le_{abu}} \tag{29}$$

in which $y = (\phi - 1)$ if $\phi > 1$, otherwise $y = \left(\frac{1}{\phi} - 1\right)$, being ϕ the equivalence ratio. The Zel'dovich number Ze is that of Eq. 25.

As can be noticed from Eq. 26, the Lewis number of a premixed mixture defined according to Joulin and Mitani [17] can be considered a weighted average of the Lewis number values computed only with respect to the deficient and abundant reactant.

Activation Temperature Model

The activation temperature of a premixed mixture was estimated by using the slope coefficient of the modified Arrhenius-type equation proposed in [30]

$$\ln s_{u0} = c - \frac{T_{act}}{2}\frac{1}{\bar{T}_f} \tag{30}$$

where $\bar{T}_f$ is the average flame temperature defined as

$$\bar{T}_f = T_u + 0.74\,(T_{ad} - T_u) \tag{31}$$

In other words, Eq. 30 is equivalent to a line equation $y = c + ax$ which is comparable to the least-square regression line of several values of $\ln s_{u0}$ obtained at different unburned mixture temperatures T_u. In fact, $\bar{T}_f$ is only function of T_u, because at fixed mixture composition $T_{ad} = f(T_u)$.

Values of T_{act} were computed before running any numerical simulation and written into a look-up table as function of pressure (p), equivalence ratio (ϕ) and exhaust gas recirculation (EGR).

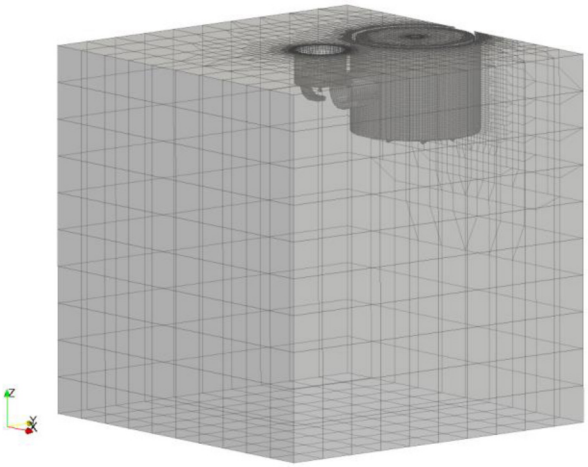

Figure 4. Pressurized combustion vessel used in Michigan Tech University for Propane-Air premixed mixture reacting tests [10]. In the upper part, it is possible to notice: the shrouded fan with the connected cylindrical guide tube, and the spark-plug.

Model Validation

The validation of the proposed comprehensive model was carried out on Michigan Tech University experimental data, concerning the flame kernel formation processes of a propane-air mixture inside a pressurized vessel [10]. Numerical simulations were performed with OpenFOAM®, an open-source platform which involves a 3-D finite volume discretization. The governing equations were solved with the RANS approach and the k-ω SST model was used for turbulence. Differently to [10], this last choice was adopted in order to improve the non-reacting flow field initialization for combustion simulations. In the following sub-sections, a description of the experimental setup configuration and of the numerical approaches used for simulations, as meshes and fan rotation simulation, were first provided. Then, non-reacting flow conditions were investigated in order to initialize the reacting test chosen for the validation and to understand the behavior of the selected turbulence model. Finally, the computed results of the combustion process were compared consistently with the available experimental findings about flame radius under different turbulence intensities, air/fuel ratios and pressures.

Experimental and Numerical Setup

A close cubic volume of 1 liter, in which a propane-air mixture is homogeneously pressurized with a suitable percentage of recycled exhaust gases (EGR), characterizes the experimental rig used by Michigan Tech University for premixed combustion tests [10]. As Figure 4 shows, inside this volume a spark-plug is present to ignite the flame, while a fan shrouded by a cylindrical shell provides a flow directed to the ignition zone through a cylindrical guide tube.

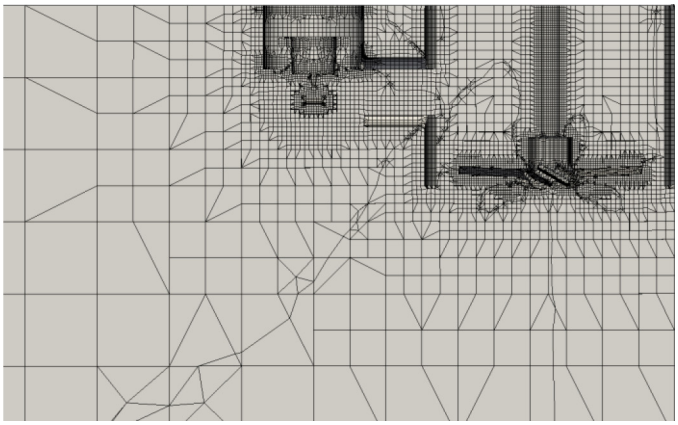

a.

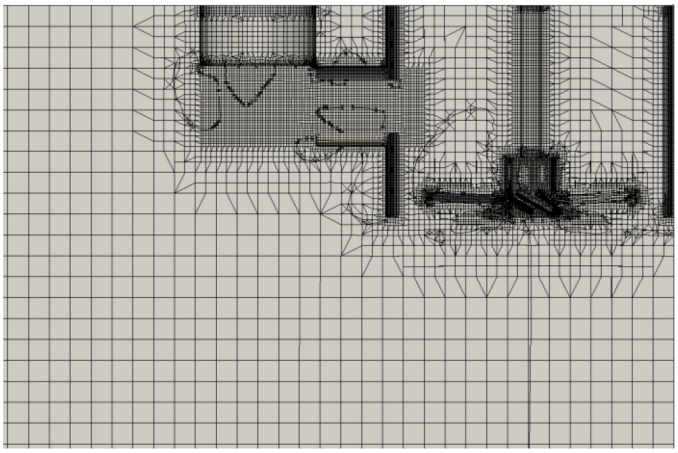

b.

Figure 5. Sectional detailed view of the adopted meshes (nearby the internal geometrical details): (a) coarse mesh for combustion simulations [10]; (b) refined mesh for PIV measurements analysis. The drawn triangles are not part of the real mesh but are simply generated by the graphics display system.

Thanks to variations of the fan speed, combustion tests cases were carried out over different turbulence levels and flow velocities, but also changes of pressure and air/fuel ratios were investigated. In addition, a PIV analysis was performed with the purpose to understand the flow field distribution at the ignition zone. Therefore, to allow PIV measurements the spark-plug was replaced by a flat cylindrical geometry, called spark-plug adapter (Figure 5b).

As shown in Figure 5, two different meshes were adopted for combustion and PIV non-reacting simulations. In the first case, the same mesh used in [10] (Figure 5a) was chosen: a basic structured grid of cubic hexahedra (10 mm side) is improved with different levels of refinement both to correctly consider the vessel geometrical details and to better describe the ignition event, where the Lagrangian

and Eulerian models are coupled. Characterized by 200000 cells, it represents a good compromise between reduced computational times and a reasonable description of the flame ignition.

On the other hand, non-reacting simulations for PIV analysis were carried out over a more refined mesh. As Figure 5b shows, in this case the basic grid was built with structured cubic hexahedra of 2.5 mm side. However, the refinement was performed consistently to the reacting cases mesh except for the ignition zone and the cylindrical guide tube, which were improved with a refinement box. According to the experimental PIV setup [10], the spark-plug was replaced by a cylindrical adapter. Approximately 400000 cells feature the resulting mesh, allowing an improved description of the flow evolution since the entering section of the guide tube.

Similarly to [10], the fan rotation simulation was handled by the Moving Reference Frame (MRF) approach, a CFD modeling technique to simulate rotating machinery. With the MRF, the momentum equation is modified to incorporate the additional Coriolis acceleration term where the part that should rotate is present. Consequently, by solving this equation, the flow around the fan could be modelled without mesh motion.

Table 2. Investigated PIV test conditions, selected form [10]. Here, P is the pressure, T the temperature, ρ the density and n the fan speed.

Test	Charged gas	P [bar]	T [K]	ρ [kg/m^3]	n [rpm]
1	Φ = 0.9 EGR = 20%	4	453	3.16	3000
2	Φ = 0.9 EGR = 20%	8	453	6.33	6000

Non-Reacting Flow Analysis

The correct initialization of reacting simulations is very important to obtain reasonable results in terms of flame propagation, because the flame interacts with the flow field and the turbulence in which it propagates. Therefore, a non-reacting flow analysis was carried out not only on the reacting test conditions chosen for the validation, but also on some flow field configurations used for PIV tests, in order to better understand the behavior of the adopted numerical setup (e.g. the turbulence model). According to [10], the PIV test conditions of Table 2 were investigated. Hence, a comparison of the numerical flow velocity magnitude and the PIV measured velocity was performed to understand the effect produced by a fan speed variation on the velocity distribution at the ignition zone. Trends were computed and measured along the linear path positioned at the spark-gap centerline and represented by the white line of Figure 6.

In Figure 7 the flow velocity distributions obtained experimentally, with the relative error bars, and numerically, by a time-averaged procedure, for the two cases of Table 2 were compared. Both trends were evaluated along the spark-gap centerline, starting from the bottom point until the flat surface of the spark-plug adapter. Despite a not perfect agreement of the numerical velocity distribution with the experimental average trend in case of a high fan speed velocity (Figures 7b), the results can be considered rather satisfactory at all tested conditions.

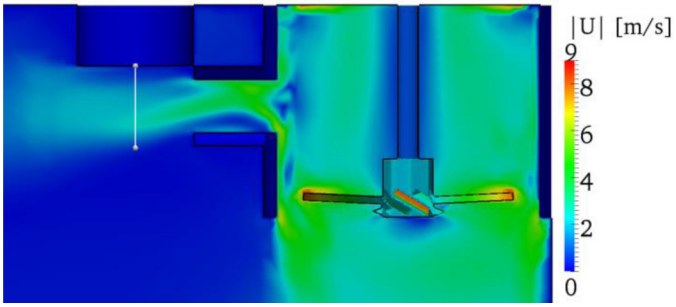

Figure 6. Instantaneous flow velocity field inside the vessel, with PIV test condition number 2 (Table 2). The experimental and numerical investigated path is represented by the white line, which is positioned at the spark-gap centerline.

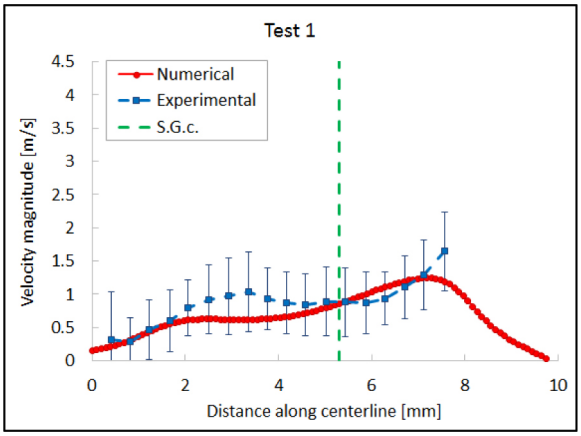

a.

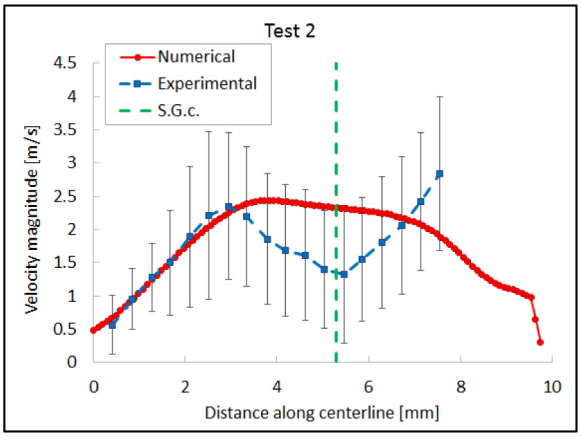

b.

Figure 7. Experimental and numerical flow velocity magnitude along the spark-gap centerline shown in Figure 6: (a) Test 1 and (b) Test 2 of Table 2. The green vertical dashed line represents the spark-gap center point (S.G.c.). The experimental data are represented with the relative error bars, while the numerical results are time-averaged values.

In fact:

1. for all the investigated tests, the average trend is quite well estimated on the region below the ignition zone;
2. for Test 2 (high fan speed) the value of the estimated flux from the spark-gap until the flat adapter falls within the confidence interval of the experimental findings (Figure 7b);
3. for Test 1 (low fan speed) the agreement between numerical and experimental values seems rather good also in terms of average trend (Figure 7a).

Concerning the initialization of combustion tests, in Table 3 the reacting conditions selected from [10] are listed and chosen for the model validation. Non-reacting simulations were carried out for each test case, in order to obtain a nearly steady-state distribution for all the involved fields and fulfill a correct initialization of the further combustion event.

Table 3. Investigated reacting test conditions, chosen from the available experimental results of [10].

Test	Charged gas	P [bar]	T [K]	ρ [kg/m^3]	n [rpm]
2	Φ = 0.7 EGR = 20%	8	453	6.21	3000
3	Φ = 0.7 EGR = 20%	8	453	6.21	6000
6	Φ = 0.7 EGR = 20%	16	453	12.42	3000
9	Φ = 0.9 EGR = 20%	8	453	6.33	6000

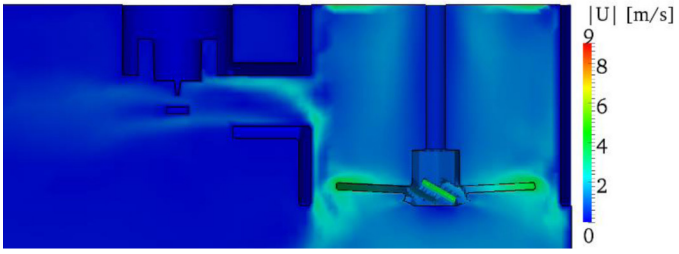

a.

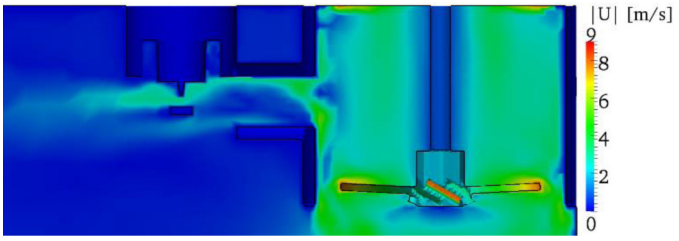

b.

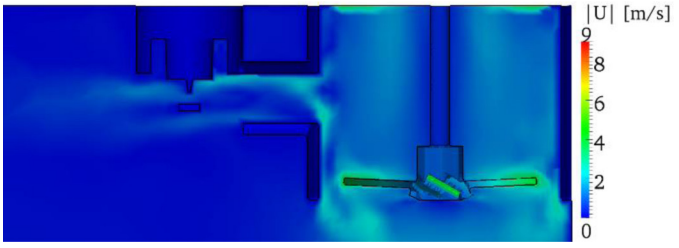

c.

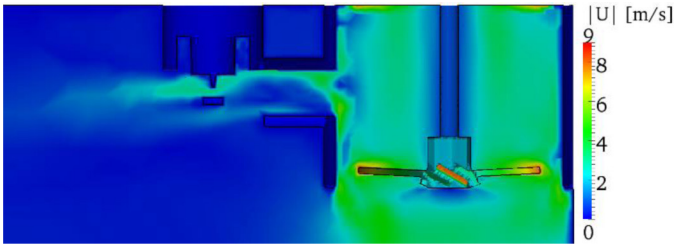

d.

Figure 8. Instantaneous flow velocity field inside the vessel before ignition (non-reacting conditions of Table 3): (a) Test 2; (b) Test 3; (c) Test 6; (d) Test 9.

Figures 8 and 9 show, for each tested condition, the distribution of the velocity and turbulence intensity fields nearby the geometrical details inside the cubic vessel, respectively. As it is possible to notice in Figure 8, the use of the k-ω SST turbulence model, combined with a rather refined mesh, allowed to predict two "fluid jets" directed towards the ignition zone: the first one hits the upper electrode and is convected at the spark-gap; the second one, of lower intensity, is directed under the bottom electrode. On the other hand, the turbulence intensity level at the ignition zone seems to be rather related to the flow velocity, and consequently to the fan speed (Figures 9a and 9b): the higher is the fan rotation velocity, the higher is the turbulence intensity at the spark-gap. However, if the fan speed is kept constant in presence of a pressure increase, both velocity and turbulence fields seem to be a little more intensive, as can be noticed be comparing Figures 8a – 8c and Figures 9a – 9c, respectively.

Combustion Results

The model validation was carried out by testing its behavior under the reactant conditions of Table 3. This choice was justified by two main reasons:

1. The Michigan Tech pressurized vessel configuration allows to study the early flame propagation under conditions of highly inhomogeneous flow field distribution nearby the ignition zone, as showed by Figures 7 and 8.
2. The four test conditions of Table 3 enable to assess the model behavior under variations of turbulence intensity (Test 2 vs. Test 3), air/fuel ratio (Test 3 vs. Test 9) and pressure (Test 2 vs. Test 6).

Therefore, once provided the near steady-state non-reacting initialization of all mixture fields (like pressure, turbulence intensity and flow velocity) for Tests 2, 3, 6 and 9, the simple ignition of each analyzed condition allowed to study the combustion phenomenon.

The electrical circuit setup was performed according to ignition system features specified in [10], considering also, for Test 6:

1. a breakdown energy of $E_{bd} = 19\ mJ$ and
2. a total released energy of $E_{tot} = 46\ mJ$, namely the global amount of energy transferred to the gas phase,

as parameters evaluated by experiments.

The parameters $\alpha_{FSD} = 30$ and $\beta_{FSD} = 0.1$ were adopted in Eqs. 19 and 20 for the Σ equation resolution, after a suitable calibration was carried out.

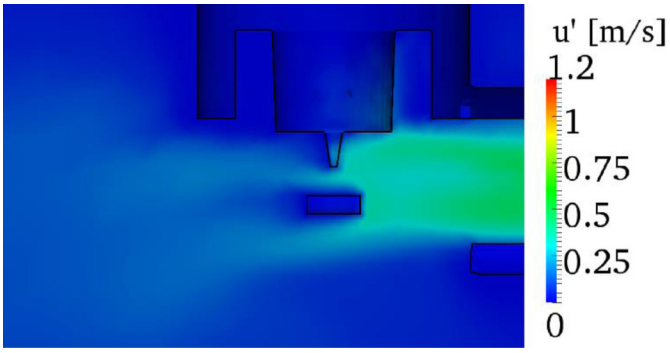

a.

Figure 9. Instantaneous turbulence intensity field inside the vessel before ignition (non-reacting conditions of Table 3): (a) Test 2; (b) Test 3; (c) Test 6; (d) Test 9.

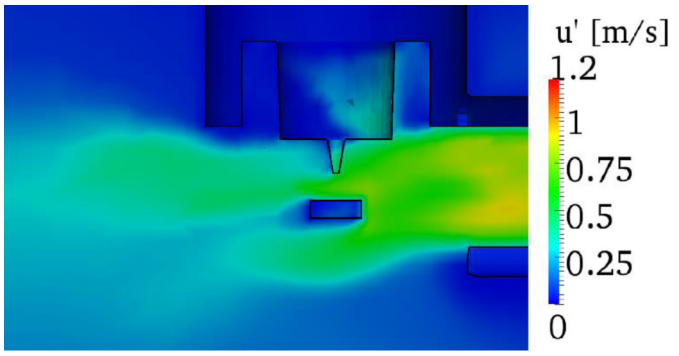

b.

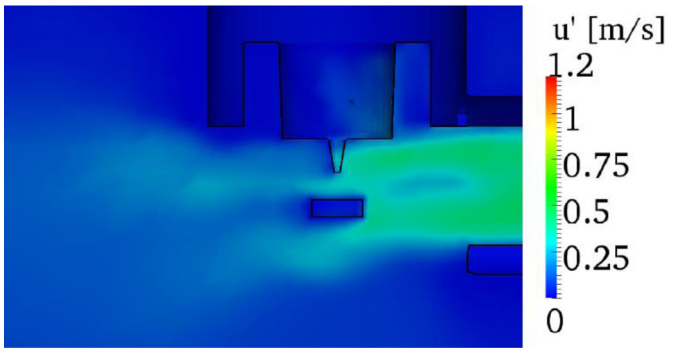

c.

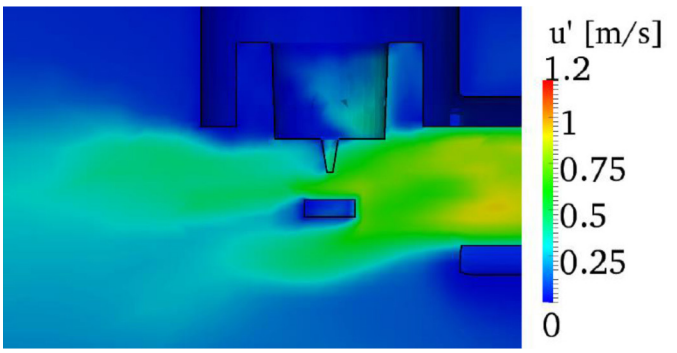

d.

Figure 9. (cont.) Instantaneous turbulence intensity field inside the vessel before ignition (non-reacting conditions of Table 3): (a) Test 2; (b) Test 3; (c) Test 6; (d) Test 9.

Simulations were performed in parallel over 3 processors with a suitable splitting of the mesh regions, in particular:

1. the cell-set used for the MRF treatment and
2. the small region around the spark-gap, where the Lagrangian-Eulerian coupling was active

were assigned each one to single cores, in order to avoid problems derived by processor boundaries. The time spent for each computation was approximately 2 days. According to [10], in order to compare consistently the obtained numerical results with the experimental evolution of the flame front position, the on-grid approach of Figure 10 was employed. The algorithm implemented for this purpose was slightly modified with respect to the one used in [10], in order to avoid possible errors due to flame front shapes similar to the Figure 10 case.

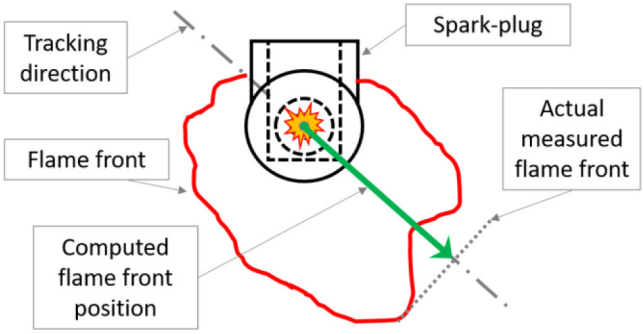

Figure 10. Simplified description of the on-grid tracking algorithm adopted for the numerical computation of the flame front position.

Figure 11 shows comparisons between experimental and numerical flame front position of Table 3 setup from the spark-time until the development of a fully turbulent flame front. Hence, for each showed comparison, the discharge event was completed before the final reported time. Rather satisfactory results were achieved at all tested conditions, especially for Test 2, 6 and 9 (Figures 11a, 11c and 11d, respectively). Concerning Test 3, also if its global propagation trend was captured, a not perfect alignment with numerical findings was observed. However, as found with the PIV analysis of Figure 7b, in presence of a 6000 rpm fan speed the predicted mean velocity profile was not perfectly achieved. Therefore, this could have a major impact on a flame propagating under lean conditions, with the consequent not perfect prediction of its evolution under such inhomogeneous flow velocity distribution. For the sake of clarity, because of:

1. numerical issues of the on-grid tracking algorithm and
2. the coarse mesh gathered by the flame outside the ignition zone,

the numerical trends of Figure 11 can sometimes show sudden but limited change of flame propagation speed.

The end time of the first discharge event (not of the total electrical discharge process) was reported in Figure 11 in order to show how much the first spark channel sustained the flame. This allowed the generation of a fully propagating turbulent flame also under such flow velocity conditions. Before the end of the discharge process, few restrike events happened with a relatively short duration. However, they did not have any effect on the generation of a self-sustained flame. More details about this are reported in Appendix C.

Concerning the flame stretch, Figure 12 shows its distribution (where it is defined as $I_0 = s_u/s_{u0}$) over the computational domain for Test 9 at three different times of the combustion process: 0.05, 0.50 and 0.95 ms. How it is possible to notice, its contribution is important during the initial stage of the kernel growth. Here, with maximum values of about 0.6, affects significantly the flame front development, reducing its propagation rate. Instead, when a self-sustained flame is developed, the flame stretch tends to asymptotically vanish, assuming values close to 1. This is mainly due to the reduction of the local flame curvature when it departs from the ignition zone.

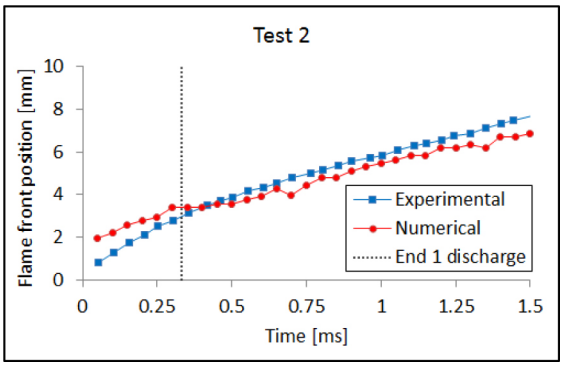

a.

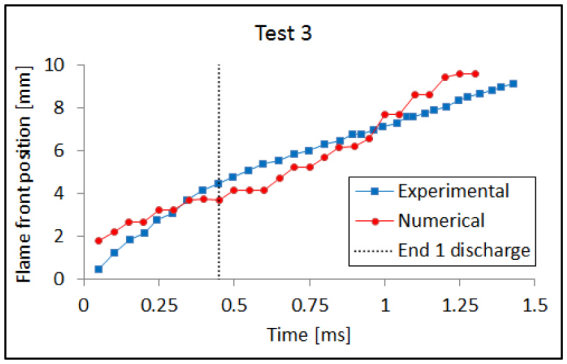

b.

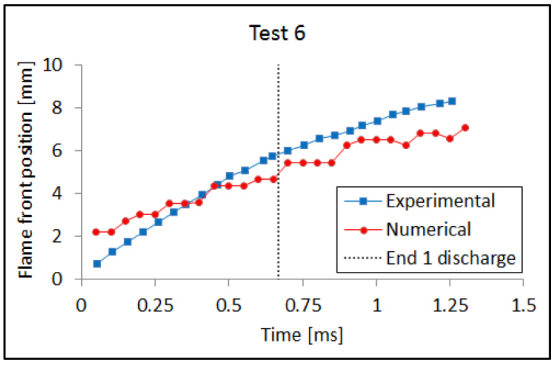

c.

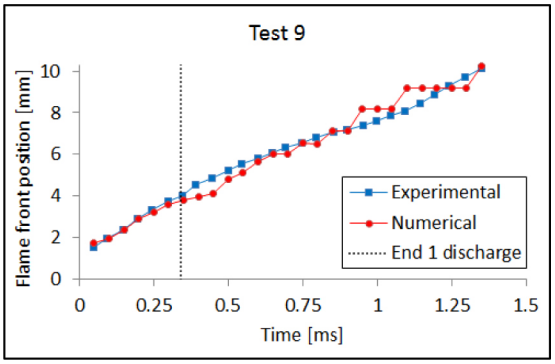

d.

Figure 11. Comparison between experimental and numerical flame front position for reacting conditions of Table 3: (a) Test 2; (b) Test 3; (c) Test 6; (d) Test 9. The black vertical dashed line represents the end of the 1st discharge.

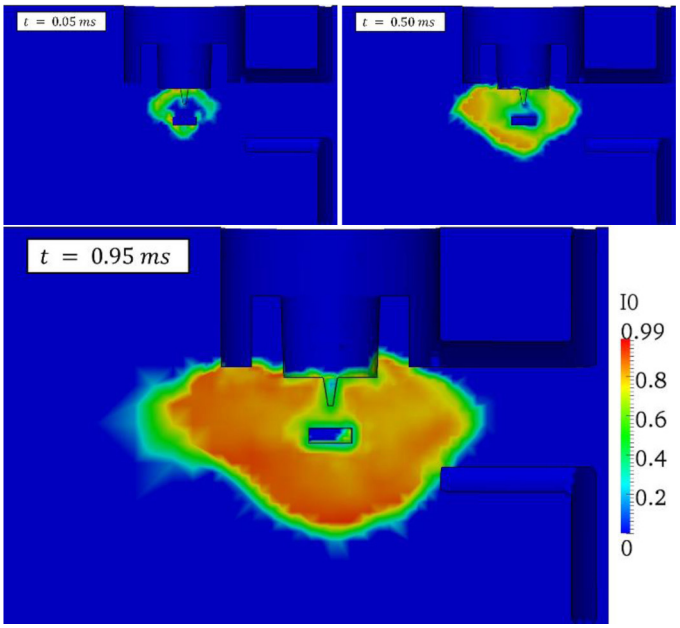

Figure 12. The flame stretch distribution of Test 9. Fields values evaluated at different times in order to show how the flame stretch evolves during the combustion process. In legend, $I_0 = s_u/s_{u0}$.

An important parameter that affects the flame stretch prediction is the Lewis number, whose distribution at three different times of the combustion process regarding Test 9 is shown by Figure 13. As can be observed, the Lewis number of a mixture of $\phi = 0.9$ assumes intermediate values between the typical Lewis numbers of propane (≈ 1.8) and air (≈ 1). Moreover, its values slightly changes according to local temperature (Figure 13, nearby the spark-gap) and pressure conditions (Figure 13, $t = 0.05$ *ms*, with pressure waves generated by the spark-event), because the diffusivities of heat, deficient reactant and abundant reactant are function of these two parameters.

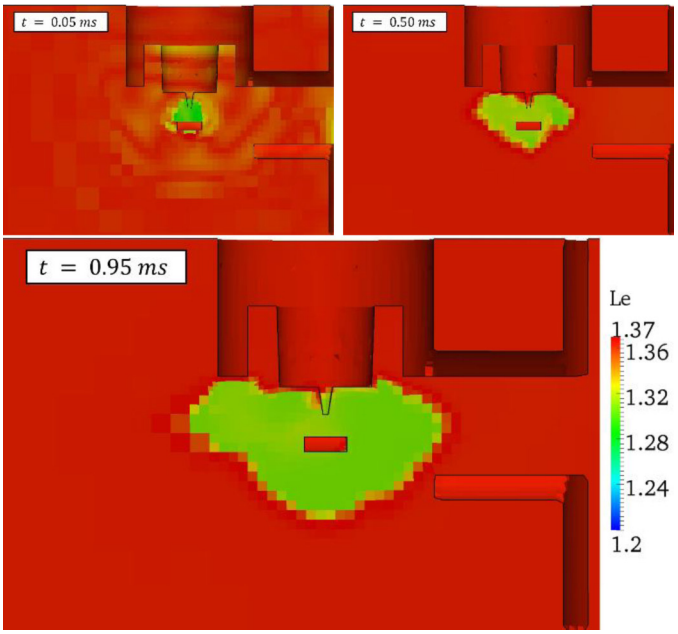

Figure 13. The Lewis number distribution of Test 9. Fields values evaluated at different times in order to show the Lewis number evolution during the combustion process.

Finally, to support the consistency of computed results, a comparison between the mixture burnt masses was carried out. As Figure 14 shows, when a self-sustained flame is developed, an increase of turbulence intensity corresponds to a faster flame front propagation (Figure 14a). On the other hand, as expected, a reduction of the mixture air/fuel ratio, namely of the equivalence ratio ϕ, generates a slower flame speed (Figure 14b). In presence of a pressure increase, Figure 14c shows that, as soon as a fully turbulent flame is formed, under conditions of ϕ = 0.7 and fan speed 3000 *rpm* an higher pressure experiences a faster flame front propagation. The much higher kernel dimension formed in Test 6 during the first breakdown event (see Eq. 2 considering that $E_{bd,Test6} = 19\ mJ > 5.19\ mJ = E_{bd,Test2}$, [10]) could explain this effect. In fact, when the dimension of the kernel structure is larger than a threshold value, a higher pressure will enhance the propagation rate [10].

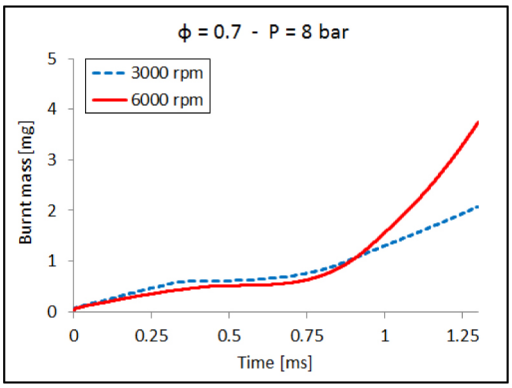

a.

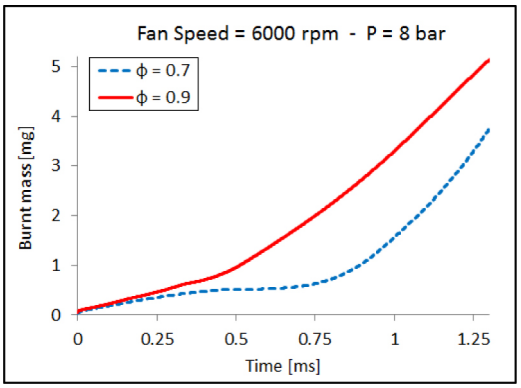

b.

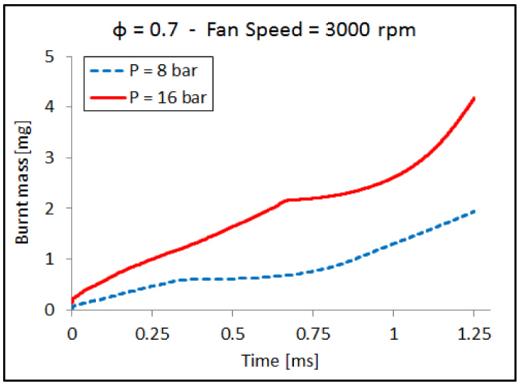

c.

Figure 14. Comparison between numerical burnt mass for reacting conditions of Table 3: (a) turbulence intensity variation (Test 2 vs. Test 3); (b) equivalence ratio variation (Test 3 vs. Test 9); (c) pressure variation (Test 2 vs. Test 6).

Another comparison between the numerical and the experimental trends of the flame front position was performed. Variations of turbulence intensity, equivalence ratio and pressure were tested: the resulting trends were rather well similar one to each other, fact that support again the validity of the implemented combustion model. For further details, see Appendix C.

Conclusions and Future Developments

The work described in this paper was focused on the implementation of a modified strategy to include flame stretch effects into ignition and premixed combustion modelling. This was performed by fully decoupling the thermal effects of the electrical circuit (still modelled by Lagrangian particles) from the chemical contribution of the laminar/turbulent flame speed. This last aspect was completely carried out by the Eulerian CFD solver, where a flame stretch model, recently verified by DNS studies, was included. Performed modifications included the effective Lewis number prediction for a premixed mixture and the electrical circuit modeling.

The proposed approach was validated using experimental data from the Michigan Tech, pressurized, constant-volume vessel under different conditions of turbulence, air/fuel ratio and pressure. First, a non-reacting flow analysis was performed:

1. to initialize the flow field for combustion calculations, and
2. to verify the proposed CFD setup in terms of turbulence model.

Regarding this last aspect, despite a not perfect agreement between PIV numerical and experimental trends under high fan speed velocities, the results could be considered rather satisfactory at all tested conditions. Concerning the initialization of combustion tests, the use of k-ω SST turbulence model, combined with a rather refined mesh, allowed to predict an additional “fluid jet” directed towards the bottom side of the spark-gap. This phenomenon was not estimated in a previous work, where simulations were carried out in a relatively coarse mesh with the k-ε turbulence model. Finally, combustion simulations was carried out. The computed results were compared consistently with the experimental data and rather satisfactory results were achieved for all tested conditions. With respect to a previous analysis, here, Test 3 (Table 3) results had no more problems of velocity propagation. The only issue was a not perfect prediction of its flame evolution, but its global trend of propagation rate was well captured.

In agreement with previous works on such topic, it was found that flame stretch mainly influences combustion development in its early propagation stage, while its effects vanish afterwards.

Finally, a comparison between the mixture burnt masses was carried out. As expected, when a self-sustained flame was developed, an increase of turbulence intensity corresponded to a faster flame front propagation, while a reduction of equivalence ratio produced a slower flame speed. Moreover, in presence of a pressure increase and under conditions of ϕ = 0.7 and fan speed 3000 *rpm*, a faster flame front propagation appeared. Regarding this observation, a much higher kernel dimension formed during the first breakdown event of the high-pressure setup could explain this phenomenon. Indeed, when the dimension of the kernel structure is larger than a threshold value, a higher pressure enhances the propagation rate.

From the achieved results, it is possible to conclude that the proposed model can be successfully applied to simulate the combustion in actual SI engines, also when turbulence and velocity conditions at the spark gap are highly inhomogeneous. Moreover, thanks to modifications of the ignition system model, also innovative ignition strategies could be tested and developed.

Despite in this work only the average combustion cycle was described, because of the use of a RANS model for turbulence, the applied numerical approach is general. Therefore, the stochastic nature of large scale eddies inside the in-cylinder flow can be considered by the use of a LES turbulence modelling. This would consequently provide the possibility to simulate and predict the cyclic combustion variability (CCV), a major issue in IC engines.

References

1. Herweg, R. and Maly, R., "A Fundamental Model for Flame Kernel Formation in S. I. Engines," SAE Technical Paper 922243, 1992, doi:10.4271/922243.
2. Tan, Z. and Reitz, R., "Modeling Ignition and Combustion in Spark-ignition Engines Using a Level Set Method," SAE Technical Paper 2003-01-0722, 2003, doi:10.4271/2003-01-0722.
3. Duclos, J. M. and Colin, O., "Arc and Kernel Tracking Ignition Model for 3D Spark-Ignition engine calculations," Proceedings of COMODIA:343-350, Nagoya, 2001.
4. Falfari, S. and Bianchi, G., "Development of an Ignition Model for S.I. Engines Simulation," SAE Technical Paper 2007-01-0148, 2007, doi:10.4271/2007-01-0148.
5. Colin, O. and Benkenida, A., "The 3-Zones Extended Coherent Flame Model (ECFM3Z) for Computing Premixed/Diffusion Combustion," *Oil & Gas Science and Technology* 59(6):593-609, 2004.
6. Dahms, R., Fansler, T.D., Drake, M.C., Kuo, T.-W. et al., "Modeling ignition phenomena in spray-guided spark-ignited engines," Proceedings of the Combustion Institute 32(2):2743-2750, 2009.
7. Dahms, R., Drake, M.C., Fansler, T.D., Kuo, T.-W. et al., "Understanding ignition processes in spray-guided gasoline engines using high-speed imaging and the extended spark-ignition model SparkCIMM. Part A: Spark channel processes and the turbulent flame front propagation," *Combustion and Flame* 158(11): 2229-2244, 2011.
8. Dahms, R., Drake, M.C., Fansler, T.D., Kuo, T.-W. et al., "Understanding ignition processes in spray-guided gasoline engines using high-speed imaging and the extended spark-ignition model SparkCIMM. Part B: Importance of molecular fuel properties in early flame front propagation," *Combustion and Flame* 158(11): 2245-2260, 2011.
9. Lucchini, T., Cornolti, L., Montenegro, G., D'Errico, G. et al., "A Comprehensive Model to Predict the Initial Stage of Combustion in SI Engines," SAE Technical Paper 2013-01-1087, 2013, doi:10.4271/2013-01-1087.
10. Zhu, X., Sforza, L., Ranadive, T., Zhang, A. et al., "Experimental and Numerical Study of Flame Kernel Formation Processes of Propane-Air Mixture in a Pressurized Combustion Vessel," *SAE Int. J. Engines* 9(3):1494-1511, 2016, doi:10.4271/2016-01-0696.
11. Peters, N., "Turbulent combustion," Cambridge university press, 2000.
12. Choi, C. R. and Huh, K. Y., "Development of a Coherent Flamelet Model for a Spark- Ignited Turbulent Premixed Flame in a Closed Vessel," *Combustion and Flame* 114:336-348, 1998, doi: 10.1016/S0010-2180(97)00194-6.
13. Fansler, T., Reuss, D., Sick, V. and Dahms, R., "Combustion instability in spray-guided stratified-charge engines: A review," *International Journal of Engine Research* 16(3):260-305, 2015.
14. Giannakopoulos, G.K., Gatzoulis, A., Frouzakis, C.E., Matalon, M. et al., "Consistent definitions of “Flame Displacement Speed” and “Markstein Length” for premixed flame propagation," *Combustion and Flame* 162(4):1249-1264, 2015.
15. Bradley, D., Lau, A.K.C. and Lawes, M., "Flame stretch rate as a determinant of turbulent burning velocity," Philosophical Transactions R. Soc. Lond. A: Physical Sciences and Engineering 338:359-387, 1992.
16. Sforza L., Lucchini T., Onorati A., "CFD Modelling of Flame Stretch in SI Engines," Energy Procedia 82:59-66, 2015, doi:10.1016/j.egypro.2015.11.883
17. Joulin, G. and Mitani, T., "Linear stability analysis of two-reactant flames," *Combustion and flame* 40:235-246, 1981, doi:10.1016/0010-2180(81)90127-9.
18. Refael, S. and Sher, E., "A theoretical study of the ignition of a reactive medium by means of an electrical discharge," Combustion and Flame 59(1):17-30, 1985, doi:10.1016/0010-2180(85)90054-9.
19. Song, J. and Sunwoo, M., "A Modeling and Experimental Study of Initial Flame Kernel Development and Propagation in SI Engines," SAE Technical Paper 2000-01-0960, 2000, doi:10.4271/2000-01-0960.
20. Nordin, N., "Complex Chemistry Modeling of Diesel Spray Combustion," Ph.D. thesis, Department of Thermo Fluid Dynamics, Chalmers University of Technology, 2001.
21. Willems, H. and Sierens, R., "Modeling the Initial Growth of the Plasma and Flame Kernel in SI Engines," *Journal of Engineering for Gas Turbines and Power* 152(2):479-484, 2003, doi:10.1115/1.1501912.
22. D'Angola, A., Colonna, G., Gorse, C., Capitelli, M., "Thermodynamic and transport properties in equilibrium air plasmas in a wide pressure and temperature range," *The European Physical Journal D* 46(1):129-150, 2008, doi:10.1140/epjd/e2007-00305-4.
23. Pashley, N., Stone, R., and Roberts, G., "Ignition System Measurement Techniques and Correlations for Breakdown and Arc Voltages and Currents," SAE Technical Paper 2000-01-0245, 2000, doi:10.4271/2000-01-0245.
24. Kim, J. and Anderson, R., "Spark Anemometry of Bulk Gas Velocity at the Plug Gap of a Firing Engine," SAE Technical Paper 952459, 1995, doi:10.4271/952459.
25. Metghalchi, M. and Keck, J. C., "Laminar burning velocity of propane-air mixtures at high temperature and pressure," *Combustion and Flame* 38:143-154, 1980, doi:10.1016/0010-2180(80)90046-2.

26. Metghalchi, M. and Keck, J. C., "Burning velocities of mixtures of air with methanol, isooctane, and indolene at high pressure and temperature," *Combustion and Flame* 48:191-210, 1982, doi:10.1016/0010-2180(82)90127-4.
27. Gülder, Ö., "Correlations of Laminar Combustion Data for Alternative S.I. Engine Fuels," SAE Technical Paper 841000, 1984, doi:10.4271/841000.
28. Bouvet, N., Halter, F., Chauveau, C. and Yoon, Y., "On the effective Lewis number formulations for lean hydrogen/hydrocarbon/air mixtures," *International Journal of Hydrogen Energy* 38(14):5949-5960, 2013, doi:10.1016/j.ijhydene.2013.02.098.
29. Poinsot, T. and Veynante, D., "Theoretical and Numerical Combustion," R. T. Edwards, 2005.
30. Brinzea, V., Razus, D., Mitu, M. and Oancea, D., "Overall activation energy of propane-air combustion in laminar flames," Ars Docendi Publishing House 1:35-41, 2009.
31. Cobine, J. D., "Gaseous Conductors: Theory and Engineering Applications," Dover publications, 1958.
32. National Institute of Standards and Technology, "Nitrogen," U.S. Department of Commerce, http://webbook.nist.gov/cgi/cbook.cgi?ID=C7727379&Mask=20
33. Michaelson, H. B., "The work function of the elements and its periodicity," *Journal of Applied Physics* 48(11):4729-4733, 1977, doi:10.1063/1.323539.

Contact Information

Lorenzo Sforza, M.Sc.
Politecnico di Milano – Department of Energy – ICE group
Via Lambruschini - 4a
20156 Milano - Italy
lorenzo.sforza@polimi.it
Phone: +39 02 2399 3909
http://www.engines.polimi.it

APPENDIX

A. MODELLING OF INTER-ELECTRODE VOLTAGE FALL V_{IE}

A particular attention was employed to model the inter-electrode voltage fall V_{IE} (Eq. 17), because different modelling approaches should be adopted during arc and glow stages. As described in [23-24], the arc mode is usually characterized by a low voltage ($V_{IE} < 100$ *V*) while, conversely, the glow phase presents higher voltages ($V_{IE} > 200$ *V*) to allow an increase of electron emission. Consequently, the voltage falls of Eq. 17 were modelled as explained in the next two subsections, assuming:

- *Air* as the gaseous conductor between the electrodes. This assumption was performed in absence of detailed experiments regarding spark discharge into fuel/air mixtures, but in the near future, a more suitable approach will be investigated.
- *Nichel* as the electrodes metal, considered a quite common used material.

Table A.1. Electrons emitted from metals per impacting positive ion γ [electron/ion]. Part of the table reported in [31] including some commonly used metals and gaseous conductors.

Metal	Air	Argon - Ar	Hydrogen – H_2
Aluminum - Al	0.035	0.12	0.095
Copper - Cu	0.025	0.058	0.05
Nichel - Ni	0.036	0.058	0.053
Platinum - Pt	0.017	0.058	0.02

ARC STAGE

This stage, characterized by a quite low voltage value and a relatively short duration (of the order of μs), required the following modelling strategy.

Cathode voltage fall V_{cf}: it is of the order of the primary ionization potential of the gas or vapor in which the arc burns. This is markedly lower than the cathode drop of potential of the glow discharge and for air can be estimated as $V_{cf,arc} = 15.8$ *V*, [31]. This value is also confirmed by NIST data about primary ionization potential of N_2, because very close to it [32].

Anode voltage fall V_{af}: estimated by Cobine [31] through the following equation

$$V_{af,arc} = \frac{H_a}{j} - \phi_0 \tag{A.1}$$

where H_a is the heat received by the anode, j the anode current density and ϕ_0 the electrodes metal work function. For Nichel-based electrodes material Kim [24] proposed the ratio $H_a/j = 13.6$ *V*, while Michaelson [33] $\phi_0 = 5.15$ *V*.

Gas-column voltage fall V_{gc}: computed according to Kim [24] by using the equation

$$V_{gc,arc}(t) = a_{gc}\, l_{spark}(t)\, i_s^{b_{gc}}(t)\, p^{c_{gc}} \tag{A.2}$$

with l_{spark} being the spark channel length in [mm], p the pressure in [bar] and $a_{gc} = 6.31$, $b_{gc} = -0.75$ and $c_{gc} = 0.51$ the coefficients for the arc stage.

GLOW STAGE

The glow stage is typical of long duration discharges (of the order of *ms*) and experiences higher voltage values with respect to the arc stage ones, as a consequence of the increased electron emission. Therefore, the implemented modelling strategy of Eq. 17 parameters is as follows.

Cathode voltage fall V_{cf}: Cobine [31] proposed this equation

$$V_{cf,glow} = \frac{3B}{A} \ln\left(1 + \frac{1}{\gamma}\right) \tag{A.3}$$

which predicts a cathode drop of potential significantly higher than the arc stage one. Here, γ represents the electrons emitted from the cathode metal per impacting positive ion and its value, according to Table A.1, can be assumed equal to 0.036. Instead, the parameters A and B are those of the Townsend equation applied with air, where A = 14.6 and B = 365, as reported in Table A.2.

Anode voltage fall V_{af}: according to [31], Eq. A.1 holds also for the glow stage.

Gas-column voltage fall V_{gc}: as suggested in [24], Eq. A.2 is valid also for the glow phase but with different coefficients: a_{gc} = 40.46, b_{gc} = -0.32 and c_{gc} = 0.51.

Table A.2. Constants of the Townsend equation. Part of the table reported in [31] including the constants related to Table 1 gaseous conductors.

Gaseous Conductor	A	B
Air	14.6	365
Argon - Ar	13.6	235
Hydrogen - H_2	5	130

B. ELECTRICAL CIRCUIT MODEL VALIDATION

The validation of the proposed electrical circuit model was carried out over two different electrical circuit systems:

1. The Transistor Coil Ignition System (TCI), characterized by long discharge times (of the order of *ms*).
2. The Capacitor Discharge Ignition System (CDI), characterized by a short discharge duration (μs) because equipped with a lower inductance value with respect to TCI systems.

This allowed to assess the capability of the model to predict completely different spark events. In fact, the TCI ignition system provides the majority of the energy transfer during the glow discharge (long discharge duration), while the CDI system operates mainly during the arc stage, thanks to its short discharge time. Herweg and Maly [1] provided useful experimental data about the aforementioned ignition systems.

TCI SYSTEM

The behavior of the proposed electrical circuit model was tested with a variation of the spark-gap mean flow velocity (Figure B.1) after being calibrated to fit the TCI system adopted by Herweg and Maly [1] (Figure B.2).

The calibration of the model was carried out trying to obtain the best fit of the available trends for:

1. Secondary circuit current i_S
2. Inter-electrode voltage V_{IE}
3. Electrical energy supplied to the mixture E_{spark}

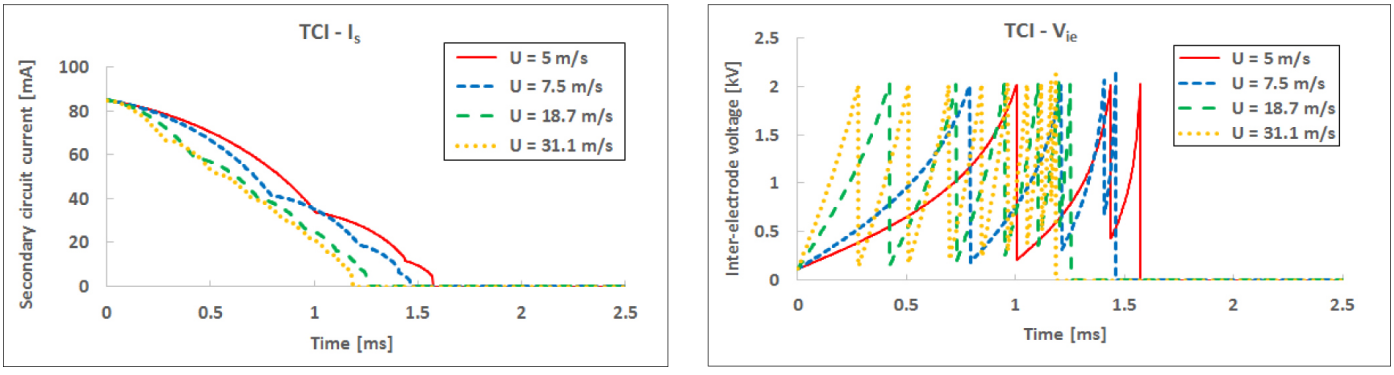

Figure B.1. TCI ignition system numerical results with a variation of mean velocity at the spark-gap. Here are showed trends for the secondary circuit current I_S and the inter-electrode voltage V_{IE}.

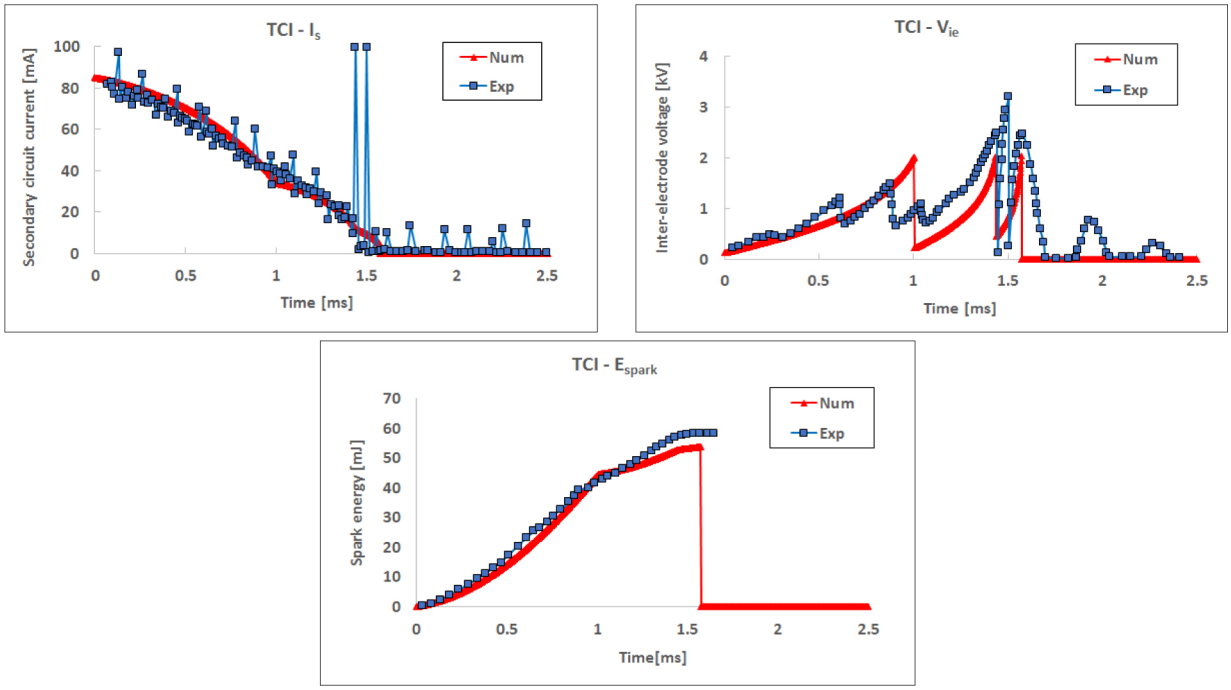

Figure B.2. Results of the calibration procedure carried out for the TCI ignition system. Comparison between experimental data from [1] and numerical results after model calibration for: the secondary circuit current I_S, the inter-electrode voltage V_{IE} and the energy released to the mixture E_{spark}.

Figure B.2 shows almost satisfactory results for all the investigated parameters; in particular, a mean flow velocity of $U = 5\ m/s$ was imposed at the spark-gap, in order to allow a correct fit.

Table B.1. Experimental and numerical discharge duration for a TCI system with different mean flow velocities at the spark-gap. The experimental data come form Herweg and Maly [1].

Mean flow velocity at the spark-gap $[m/s]$	**Discharge duration $[ms]$**	
	Experimental	**Numerical**
7.5	1.2	1.5
18.7	0.9	1.3
31.1	0.7	1.2

Afterwards, the sensitivity of the model was tested under different flow velocities at the spark-gap. The results of Figure B.1 allows to assert that, with an increase of the mean flow velocity:

1. The discharge duration is reduced
2. The number of restrike events is increased

This is in accordance to the experimental trend reported in Table B.1, but also with other experimental findings [24].

CDI SYSTEM

As performed for the TCI system, the implemented electrical circuit model was tested with different gas flow velocities at the spark-gap (Figure B.3) after a calibration procedure (Figure B.4), carried out to fit the Herweg and Maly [1] CDI system behavior.

As Figure B.4 shows, after a suitable calibration which included the assumption of $U = 5\ m/s$ at the spark-gap, the experimental trends for secondary circuit current i_S, inter-electrode voltage V_{IE} and electrical energy supplied to the mixture E_{spark} were well captured by the proposed model.

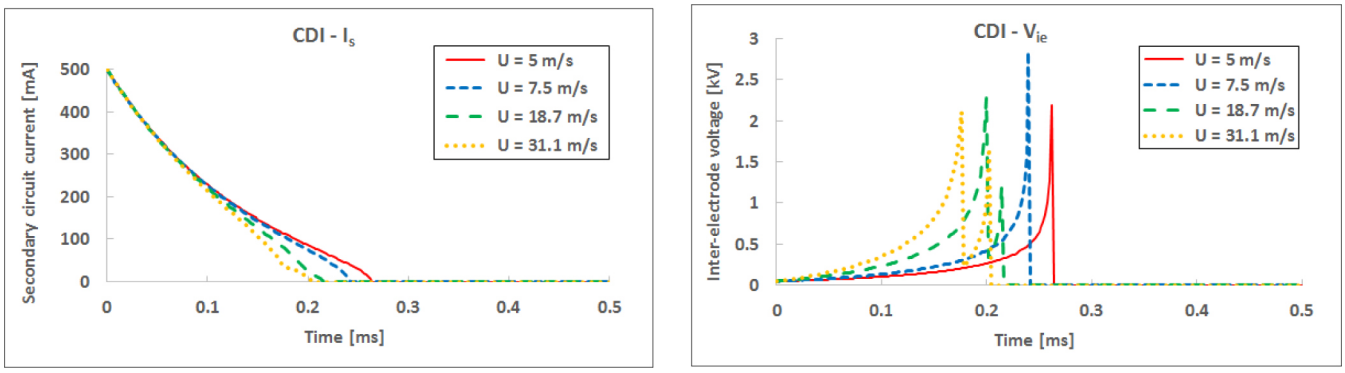

Figure B.3. CDI ignition system numerical results with a variation of mean velocity at the spark-gap. Here are showed trends for the secondary circuit current I_S and the inter-electrode voltage V_{IE}.

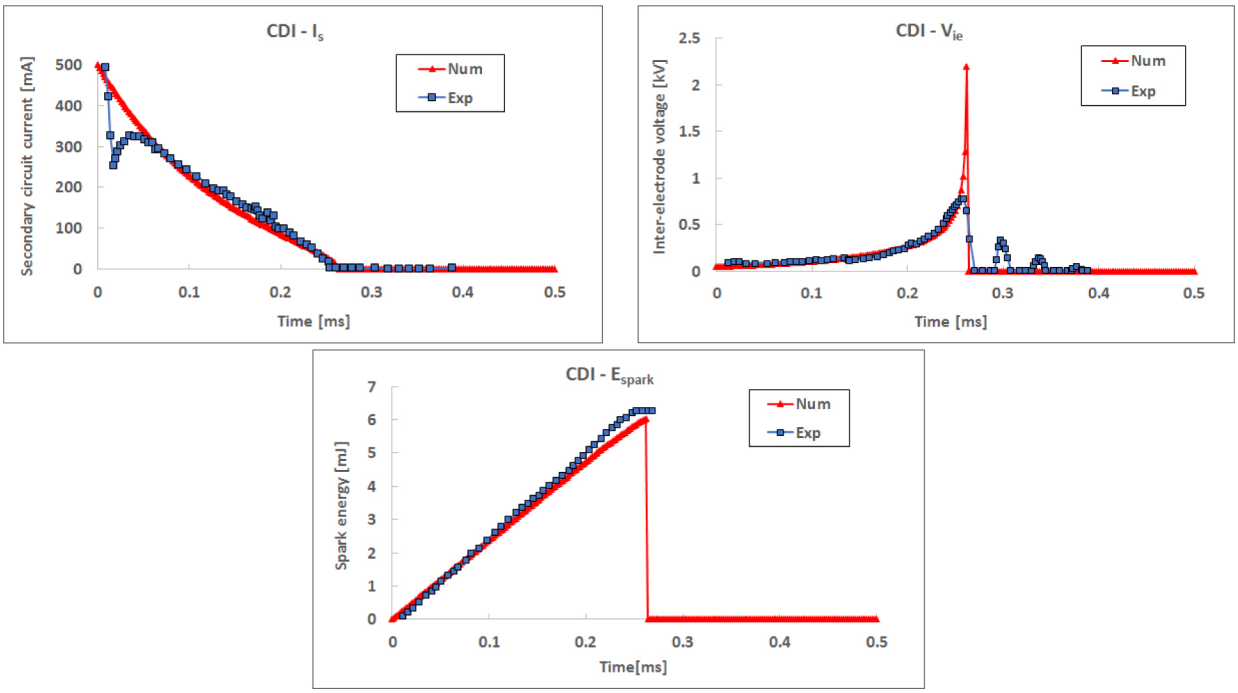

Figure B.4. Results of the calibration procedure carried out for the CDI ignition system. Comparison between experimental data from [1] and numerical results after model calibration for: the secondary circuit current I_S, the inter-electrode voltage V_{IE} and the energy released to the mixture E_{spark}.

Concerning the investigation on the model sensitivity to a flow velocity variation at the spark-gap, Figure B.3 togheter with Table B.2 allows to conclude that, in presence of an increase of the flow velocity, the:

1. Reduction of discharge duration
2. Increase of the restrike events number

are well captured. In particular, the first mentioned phenomenon was predicted with very good agreement also form a quantitative point of view (Table B.2).

Table B.2. Experimental and numerical discharge duration for a CDI system with different mean flow velocities at the spark-gap. The experimental data come form Herweg and Maly [1].

Mean flow velocity at the spark-gap $[m/s]$	**Discharge duration $[ms]$**	
	Experimental	**Numerical**
7.5	0.24	0.24
18.7	0.22	0.22
31.1	0.20	0.20

C. COMPLEMENTS TO COMBUSTION RESULTS

In this section, the achieved combustion results were further explained by the use of additional images and comparisons. Firstly, the coupling of the Lagrangian and Eulerian model was showed along a complete ignition process, in order to understand how the fully decoupling of electrical circuit heat transfer and chemical flame development worked. Finally, a comparison between experimental and numerical trends under variations of turbulence, air/fuel ratio and pressure was proposed.

IGNITION AND DEVELOPMENT OF A SELF-SUSTAINED FLAME

The complete ignition process and the further development of a self-sustained flame is showed in Figure C.1, where the Test 9 of Table 3 was chosen as example. As soon as the first spark channel ended (before $t = 0.35$ *ms*), a self-sustained flame was generated also under such inhomogeneous flow conditions. Before the end of discharge process, few restrike events happened with a relatively short duration. However, they did not have any effect on the generated flame.

In Figure C.1, the spatial evolution of the first spark channel cannot be well identified. This is due to the relatively high energy deposited during the breakdown stage of Test 9 first discharge, which generated a mean Lagrangian particles radius of about 1 *mm* at the beginning of the arc stage [10]. Being this value comparable to the spark-gap distance (1.4 *mm*), it is very difficult to understand the effects of the local flow field on the channel geometry if the actual particles radius is represented into the computational domain.

Hence, as showed in Figure C.2, a factor of 10 was used to artificially decrease the Lagrangian particles dimension in order to better analyze all spark-channels behavior. As can be noticed from Figure C.2, all spark-channel paths were strongly influenced by the local flow field distribution, also if during the first discharge the actual particles dimensions (Figure C.1) seem to create a near-spherical flame shape.

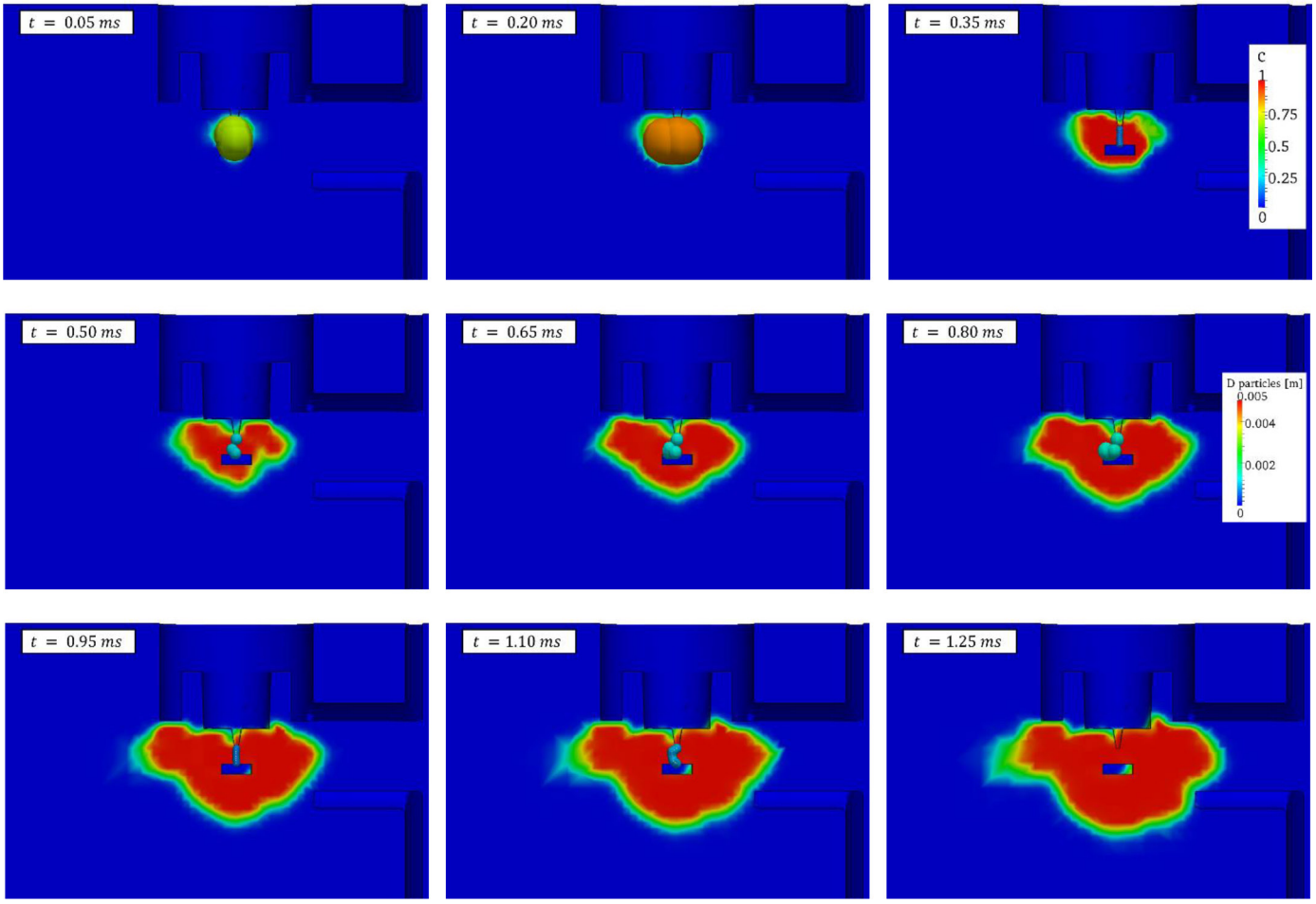

Figure C.1. The Lagrangian-Eulerian coupling from ignition until self-sustained flame, Test 9 of Table 3. At these conditions, the restrike events experienced after the completion of the first discharge does not influence the formation of a self-sustained propagating flame.

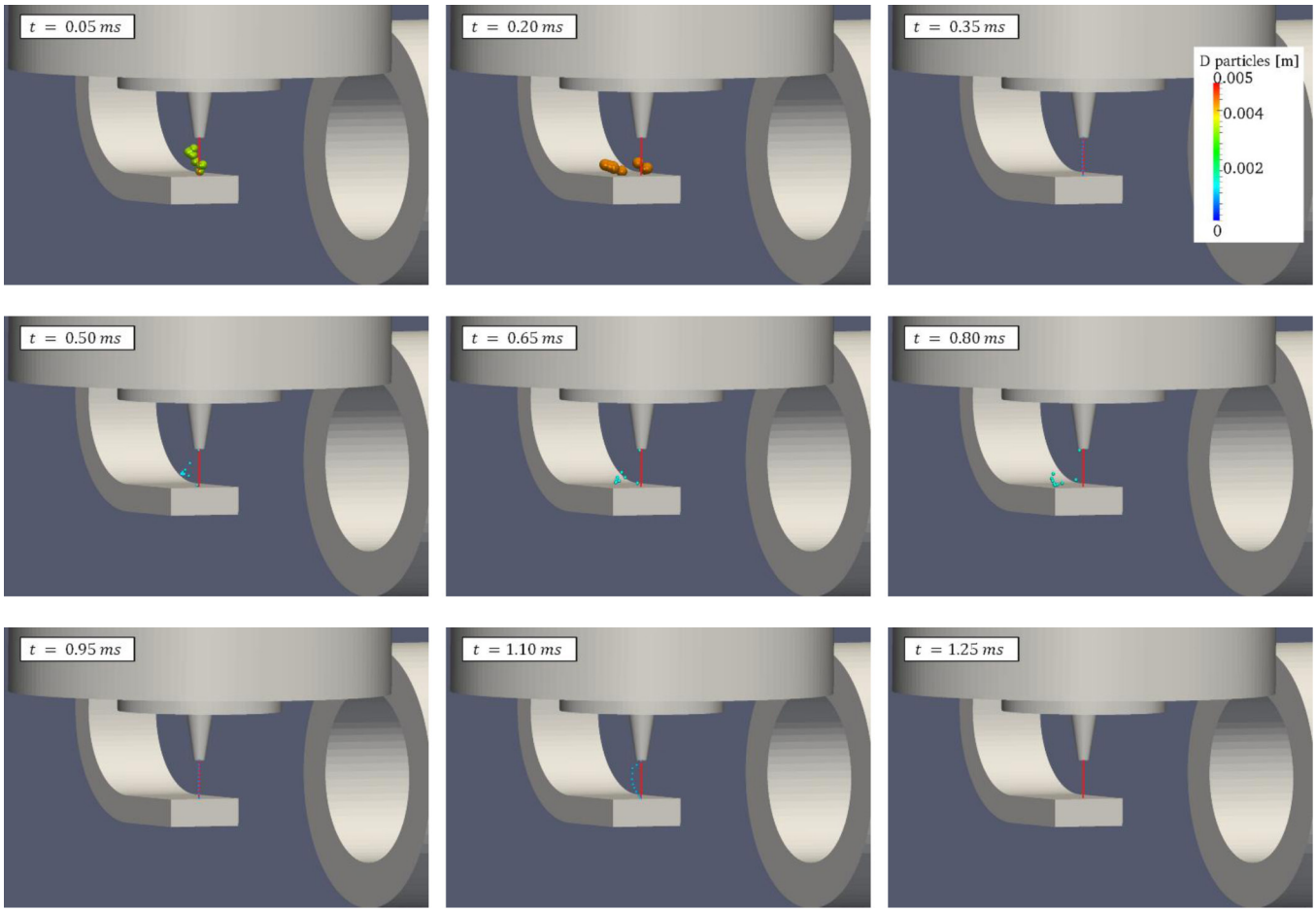

Figure C.2. The distribution of the Lagrangian particles at the same time-steps of Figure C.1. Here, the actual dimension of each particle was reduced of a factor of 10 in order to appreciate their actual position. The bold red line represents the spark-gap centerline.

NUMERICAL VS. EXPERIMENTAL TRENDS

To understand in deep if consistency was achieved between computed results and available experimental findings, comparisons between experimental and numerical trends of the flame front position were carried out under variations of:

1. Turbulence (Figure C.3).
2. Air/fuel ratio, or equivalence ratio (Figure C.4).
3. Pressure (Figure C.5).

As it is possible to notice, the results are quite satisfactory at all investigated variations.

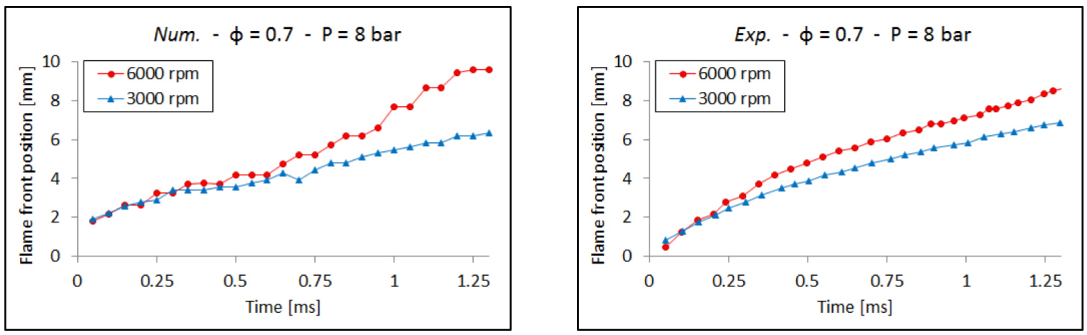

Figure C.3. Comparison between numerical (left) and experimental (right) trends of flame front position under a turbulence variation. For each chart, Test 2 vs. Test 3 of Table 3 were used.

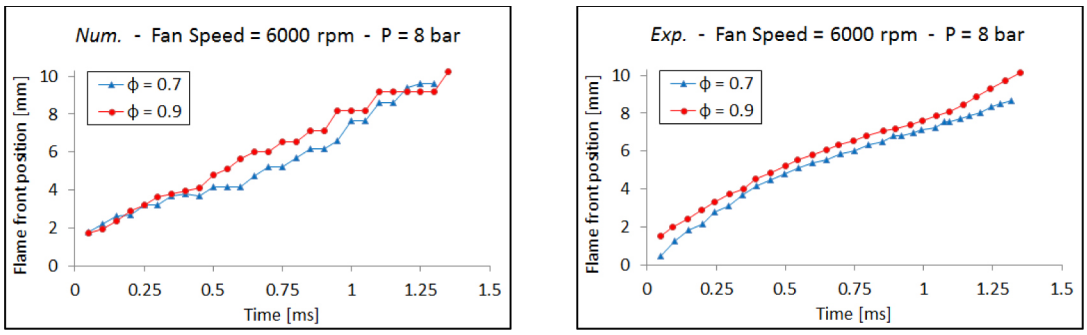

Figure C.4. Comparison between numerical (left) and experimental (right) trends of flame front position under an equivalence ratio variation. For each chart, Test 3 vs. Test 9 of Table 3 were used.

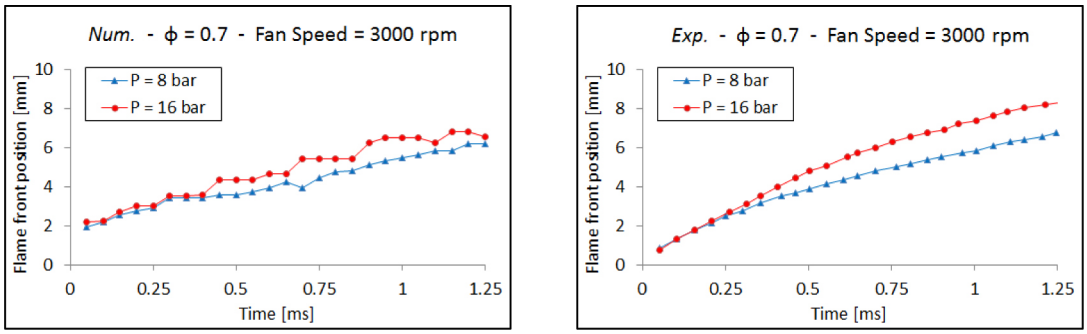

Figure C.5. Comparison between numerical (left) and experimental (right) trends of flame front position under a pressure variation. For each chart, Test 2 vs. Test 6 of Table 3 were used.

ISSN 0148-7191

http://papers.sae.org/2017-01-0553